2012

Electromagnetic scattering in a discrete basis

Christopher Paul Trampel
Iowa State University

Electromagnetic scattering in a discrete basis

by

Christopher Paul Trampel

A dissertation submitted to the graduate faculty

in partial fulfillment of the requirements for the degree of

DOCTOR OF PHILOSOPHY

Major: Electrical Engineering

Program of Study Committee:
John Bowler, Major Professor
Rana Biswas
Nicola Bowler
Brian Hornbuckle
Jiming Song

Iowa State University

Ames, Iowa

2012

DEDICATION

I would like to dedicate this dissertation to my beloved wife Mary. Without your patience this work would not have been possible. I am also grateful to my parents for their support during the final stages of writing. Thanks are due to my major professor, Dr. John Bowler, for many enjoyable discussions, as well as for the research assistanceship during the fall and spring semesters of 2007. Thank you to Dr. Rana Biswas, Dr. Nicola Bowler, Dr. Brian Hornbuckle, and Dr. Jiming Song for serving on my committee. A special thanks to Dr. Biswas for funding my research during the summer of 2007. Thank you also to the research and development team at PowerFilm, Inc. for funding the work that became Chapter 3 of this dissertation. Thank you all. *Propter artis suscepi.*

TABLE OF CONTENTS

LIST OF FIGURES v

CHAPTER 1 Introduction 1

CHAPTER 2 Eddy-current coil interaction with a perfectly conducting wedge of arbitrary angle 5

2.1 Literature Review 5

2.2 Scalar Decomposition 6

2.3 Fourier-Bessel Series Representation of the TE Green's Functions 8

2.3.1 Hollow Circular Waveguide 8

2.3.2 Circular sectoral waveguide 11

2.4 Potential due to a current-loop inside a circular sectoral waveguide 12

2.5 Potential due to a circular coil inside a circular sectoral waveguide 14

2.6 Impedance 15

2.7 Results and Validation 16

2.7.1 Validation 16

2.7.2 Results for wedge angles of 225 and 270 degrees 17

2.7.3 Conducting Sheet 19

2.8 Conclusion 20

CHAPTER 3 Control of electromagnetic edge effects in electrically-small rectangular plasma reactors 21

3.1 Literature Review 21

3.2 Scalar Decomposition 23

3.3 Standing Wave 24

3.4 Evanescent waves and edge effects . . . 27
3.4.1 Edge Waves . . . 27
3.4.2 Corner Wave . . . 29
3.5 Results . . . 32
3.5.1 Film Deposition . . . 32
3.5.2 Control of Nonuniformity . . . 34
3.6 Conclusions . . . 36

CHAPTER 4 Modal analysis of extraordinary optical transmission through a silver film perforated by an infinite square array of circular holes . . . 38

4.1 Literature Review . . . 38
4.2 Scalar Decomposition . . . 41
4.3 Waveguide modes . . . 42
4.4 Eigenfunction expansions . . . 45
4.4.1 Incident field . . . 45
4.4.2 Regions 1 and 3 . . . 46
4.4.3 Region 2 . . . 47
4.5 Matrix Equations . . . 48
4.6 Results . . . 50
4.7 Conclusions . . . 53

APPENDIX A Fourier-Bessel series representation of the TM Green's functions . . . 62

APPENDIX B Plasma matrix definitions . . . 66

APPENDIX C Intermediate matrix definitions . . . 69

BIBLIOGRAPHY . . . 70

LIST OF FIGURES

Figure 2.1 Finite eddy-current coil in the presence of an infinite perfectly conducting wedge. 7

Figure 2.2 Loop Geometry 12

Figure 2.3 Theoretical reactance change as a function of coil lift-off using TREE method (blue line) and Burke theory (red triangles). 17

Figure 2.4 Quarter-space Geometry. 17

Figure 2.5 Reactance variation with coil axis position relative to the vertex for wedges of angle 225 (solid line) and 270 (dashed line) degrees for coil C5 excited at 850 Hz and a lift-off of 20 mm. 18

Figure 2.6 Conducting Sheet Geometry. 19

Figure 2.7 Reactance variation with coil axis position relative to the edge of the conducting sheet for coil C5 excited at 850 Hz. 19

Figure 3.1 Cross-sectional(a) and top(b) view of plasma reactor. 24

Figure 3.2 Rotated coordinate system for corner wave. 29

Figure 3.3 Normalized theoretical power and experimental deposition thickness in the y-direction at x=$L_x/2$. The aluminum electrode of dimensions 55.8×40.6 cm^2 was center-fed by a point source on the back side. An 11:1 hydrogen to silane ratio was maintained at a base pressure of 530 mTorr for 10 minutes during the deposition. 33

Figure 3.4 Normalized theoretical power at 13.56(a) and 40.68(b) MHz. 34

Figure 3.5 Normalized theoretical power for 111.7×41.9 cm^2 electrode with bare(a) and coated(b) sidewalls. 35

Figure 3.6 Theoretical nonuniformity as a function of layer thickness(a) and normalized theoretical power for a 5 mm thick layer(b). 36

Figure 4.1 Top(a) and side(b)-view of silver film perforated by an infinite array of circular holes. The region above the film is designated 1, inside the hole 2, and below the film 3. 39

Figure 4.2 Theoretical transmission through a 320 nm thick silver film perforated by a square array of circular holes of radius 140 nm and lattice constant 750 nm at normal incidence. The transmission profile was calculated using the Drude model (black line) and experimental values (red dotted line) for the silver permittivity. 50

Figure 4.3 Theoretical extraordinary transmission through a 320 nm thick silver film perforated by an array of circular holes of radius 140 nm and lattice constant 750 nm at normal incidence from 400 to 1000 nm(a) and from 775 to 800 nm(b). 55

Figure 4.4 Normalized z-component of the electric field for the fundamental mode at a wavelength of 790 nm. The x and y-axes have been normalized by the hole radius. The panels show the real(a) and imaginary(b) parts of the field for the fundamental hybrid HEM11 mode used with an IBC on the hole wall. The remaining panels show the real(c) and imaginary(d) parts of the field for the fundamental TM11 mode used with a PEC boundary condition on the hole wall. 56

Figure 4.5 Normalized ϕ-component of the electric field for the fundamental mode at a wavelength of 790 nm. The x and y-axes have been normalized by the hole radius. The panels show the real(a) and imaginary(b) parts of the field for the fundamental hybrid HEM11 mode used with an IBC on the hole wall. The remaining panels show the real(c) and imaginary(d) parts of the field for the fundamental TM11 mode used with a PEC boundary condition on the hole wall. 57

Figure 4.6 Theoretical transmission for the film thicknesses listed in the panel. . . 58
Figure 4.7 Theoretical transmission for the hole radii listed in the panel for a 320 nm thick film with lattice constant 750 nm. 58
Figure 4.8 Theoretical transmission for the lattice constants listed in the panel for a 320 nm thick film with hole radius of 140 nm. 59
Figure 4.9 Theoretical transmission-to-area efficiency as a function of lattice constant. 59
Figure 4.10 Polarization (double arrows) and axis of rotation (dashed line) for incident field. 60
Figure 4.11 Transmission for the incident angles (in degrees) listed in the panel. . . 60
Figure 4.12 Transmission for the incident angles (in degrees) listed in the panel. . . 61

CHAPTER 1 Introduction

Classical electromagnetic scattering in the frequency-domain is described by Maxwell's equations

$$\nabla \times \mathbf{E} = -\jmath\omega\mathbf{B} \tag{1.1}$$

$$\nabla \times \mathbf{H} = \mathbf{J} + \jmath\omega\mathbf{D} \tag{1.2}$$

$$\nabla \cdot \mathbf{D} = \rho_v \tag{1.3}$$

$$\nabla \cdot \mathbf{B} = 0 \tag{1.4}$$

along with the following constitutive relations

$$\mathbf{D} = \boldsymbol{\epsilon} \cdot \mathbf{E} \tag{1.5}$$

$$\mathbf{B} = \boldsymbol{\mu} \cdot \mathbf{H} \tag{1.6}$$

$$\mathbf{J} = \boldsymbol{\sigma} \cdot \mathbf{E}. \tag{1.7}$$

Here ω is the frequency, $\jmath$ is the unit imaginary number, $\mathbf{E}$ is the electric field (V/m), $\mathbf{H}$ is the magnetic field (A/m), $\mathbf{D}$ is the electric flux density ($\mathrm{C/m^2}$), $\mathbf{B}$ is the magnetic flux density ($\mathrm{Wb/m^2}$), $\mathbf{J}$ is the current density ($\mathrm{A/m^2}$), ρ_v is the charge density ($\mathrm{C/m^3}$), V stands for volts, C for coulombs, m for meters, A for amperes, and Wb for webers. Also $\boldsymbol{\epsilon}$, $\boldsymbol{\mu}$, and $\boldsymbol{\sigma}$ are the permittivity, permeability, and conductivity tensors, respectively. Satisfying these equations subject to appropriate boundary conditions is sufficient to guarantee a unique solution.

One may reduce the vector-valued problem of solving Maxwell's equations to an equivalent scalar problem via the scalar decomposition. For a preferred direction along $\hat{\mathbf{u}}$, the electric and magnetic fields may be expressed in terms of TM (ψ) and TE (φ) scalar potentials[1]

$$\mathbf{E} = \nabla \times \nabla \times [\hat{\mathbf{u}}\psi] - \jmath\omega\mu_p \nabla \times [\hat{\mathbf{u}}\varphi] \tag{1.8}$$

$$\mathbf{H} = \jmath\omega\epsilon_p \nabla \times [\hat{\mathbf{u}}\psi] + \nabla \times \nabla \times [\hat{\mathbf{u}}\varphi] \tag{1.9}$$

where ϵ_p, μ_p are the material parameters in region p. The potentials satisfy the Helmholtz equation

$$(\nabla^2 + k_p^2)\psi = s_1(\mathbf{r}) \tag{1.10}$$

and

$$(\nabla^2 + k_p^2)\varphi = s_2(\mathbf{r}) \tag{1.11}$$

where $k_p^2 = \omega^2\epsilon_p\mu_p$ and $s_1(\mathbf{r})$ and $s_2(\mathbf{r})$ are source terms.

Appropriate expansions for the scalar potentials are essential to the analytical solutions I propose. Specifically, the set of functions must form a basis for the vector space in question. Consider a linear operator $\mathcal{L} : H \to H$ defined on an infinite-dimensional Hilbert space H. The *spectrum* of the operator $\mathcal{L}$ is defined as the set

$$\sigma(\mathcal{L}) = \{\lambda \in \mathbb{C} \mid (\mathcal{L} - \lambda\mathcal{I}) \text{ is not invertible}\}. \tag{1.12}$$

Any $\lambda \in \sigma(\mathcal{L})$ is also a member of one of three subsets

$$\sigma(\mathcal{L}) = \sigma_p(\mathcal{L}) \cup \sigma_c(\mathcal{L}) \cup \sigma_r(\mathcal{L}). \tag{1.13}$$

The *point spectrum* is defined as the set

$$\sigma_d(\mathcal{L}) = \{\lambda \mid (\mathcal{L} - \lambda\mathcal{I}) \text{ is not one-to-one}\}. \tag{1.14}$$

In this case the kernel of $(\mathcal{L} - \lambda\mathcal{I})$ is nonempty. Therefore, there exists $x_\lambda \in \ker(\mathcal{L} - \lambda\mathcal{I})/\{0\}$, that is $(\mathcal{L} - \lambda\mathcal{I})x_\lambda = 0$, $\mathcal{L}x_\lambda = \lambda x_\lambda$. Here x_λ is the eigenfunction associated with eigenvalue λ. The *continuous spectrum* is the set

$$\sigma_c(\mathcal{L}) = \left\{\lambda \mid (\mathcal{L} - \lambda\mathcal{I}) \text{ is one-to-one but not onto, and } \overline{\text{ran}(\mathcal{L} - \lambda\mathcal{I})} = H\right\}. \tag{1.15}$$

Finally, the *residual spectrum* is the set

$$\sigma_r(\mathcal{L}) = \left\{\lambda \mid (\mathcal{L} - \lambda\mathcal{I}) \text{ is one-to-one but not onto, and } \overline{\text{ran}(\mathcal{L} - \lambda\mathcal{I})} \neq H\right\}. \tag{1.16}$$

For most electromagnetics problems, the residual spectrum is empty and the point spectrum is discrete.[2] However, the discrete and continuous spectrum may both be nonempty. Specifically, the Helmholtz operator $\mathcal{H} = \nabla^2 + k_p^2$ has both a discrete and continuous spectrum

for unbounded domains. As such, both a series and integral are necessary to represent the potential

$$\psi(\mathbf{r}) = \sum_{i=1}^{\infty} D_i f_i(\mathbf{r}) + \int_{-\infty}^{\infty} C(\beta) F(\mathbf{r}) d\beta. \tag{1.17}$$

However, the following key result applies to bounded domains[3]

Theorem 1.0.1 (Spectral theorem for compact, self-adjoint operators). *Let $\mathcal{L} : H \to H$ be a compact, self-adjoint operator on a Hilbert space H. Then there is an orthonormal basis of H consisting of the eigenfunctions of $\mathcal{L}$. The nonzero eigenvalues of $\mathcal{L}$ form a finite or countably infinite set $\{\lambda_k\}$ of real numbers, and*

$$\mathcal{L} = \sum_{k} \lambda_k \mathcal{P}_k, \tag{1.18}$$

where $\mathcal{P}_k$ is the orthogonal projection onto the finite-dimensional eigenspace of eigenvectors with eigenvalue λ_k. If the number of nonzero eigenvalues is countably infinite, then the series in (1.18) converges to $\mathcal{L}$ in the operator norm.

Theorem 1.0.1 guarantees that the eigenfunctions of $\mathcal{L}$ form a basis on a finite domain. In this case, the potentials may be represented by a discrete basis

$$\psi(\mathbf{r}) = \sum_{i=1}^{\infty} D_i f_i(\mathbf{r}). \tag{1.19}$$

In this dissertation, I use discrete eigenfunction expansions to study three electromagnetic scattering problems in the frequency-domain. In Chapters 2 and 3, the $\jmath$ convention is adopted for complex numbers, while I adopt the $\imath$ convention in Chapter 4. Chapter 2 describes an eddy-current coil interacting with a perfectly conducting wedge of arbitrary angle. A closed-form expression for the impedance of a tangential eddy-current coil in the presence of an infinite conducting wedge of arbitrary angle is derived. The truncated eigenfunction expansion (TREE) solution given here is valid in the quasi-static frequency regime. The theory was validated via comparison to an independent analytical expression for the impedance change of a horizontal coil over a conducting half-space due to Burke. I present results for three geometries: a conducting quarter-space, a conducting wedge of angle 225 degrees, and a semi-infinite conducting sheet. Our theory predicts a measurable change in the tangent coil reactance in the presence of all three geometries.

Chapter 3 discusses the control of electromagnetic edge effects in electrically-small rectangular plasma reactors. Expressions for the fields in an electrically-small rectangular reactor with plasma in the chamber are derived. Modal field decompositions are employed under the homogeneous plasma slab approximation. The amplitude of each mode is determined analytically. It is shown that that the field can be represented by the standing wave, evanescent waves tied to the edges, and an evanescent wave tied to the corners of the reactor. The impact of boundary conditions at the plasma edge on nonuniformity is quantified. Uniformity may be improved by placing a lossy magnetic layer on the reactor sidewalls. It is demonstrated that nonuniformity is a decreasing function of layer thickness.

Chapter 4 is a theoretical investigation of extraordinary optical transmission (EOT) through a silver film perforated by an infinite square array of circular holes. A mode-matching solution to plane wave scattering by a silver film perforated by an infinite array of circular holes is presented. Impedance boundary conditions are imposed on all surfaces. Theory predicts a peak transmission value that is in good agreement with experiment. Extraordinary optical transmission is studied as a function of film thickness, hole radius, and lattice constant. The transmission profile position, shape, and amplitude are strong functions of film thickness, hole radius, and lattice constant. The effect of film thickness on coupling between modes bound to the upper and lower surfaces is studied. It is demonstrated that transmission peaks occur for holes of a roughly constant electrical size. A relationship between the lattice constant and the transmission-to-area efficiency is quantified. The relationship between angle of incidence and the position of transmission peaks is explored.

CHAPTER 2 Eddy-current coil interaction with a perfectly conducting wedge of arbitrary angle

2.1 Literature Review

In general, eddy-current coils are positioned with their axes perpendicular to the surface under investigation. This pancake orientation allows for good coupling between the coil and the work-piece. However, it may be advantageous to position the coil with its axis parallel to the surface, the so-called tangential orientation. While the coupling with the work-piece is weaker, tangent coils sometimes allow for better probe access. In this chapter, the interaction of a tangent coil with a perfectly conducting wedge is studied. An analytical expression for the impedance of an eddy-current coil in the presence of an infinite perfectly conducting wedge in a radially truncated domain has been derived. The axis of the coil is parallel to the edge formed by the intersection of the faces of the wedge (Figure 2.1). The problem is of interest to researchers in eddy-current non-destructive evaluation (NDE).

To find the impedance of the coil, I determine first the field scattered by a dipole in the presence of the wedge and deduce the dipole field from a Green's function. Integral representations of the Green's function for an infinite conducting wedge were determined by Felsen and Marcuvitz[4], Wait[5], and Mishustin[6]. Felsen expresses the Green's function as both a double improper integral and an improper integral and an infinite series. Wait's approach also leads to an integral with infinite limits of integration and an infinite series. Mishustin employs analytical transformations to represent the Green's function as a single integral with finite limits of integration. In order to avoid integral representations I solve for the Green's function of a conducting wedge in a radially truncated domain, expressing the result in the form of a series. This solution is equivalent to the Green's function of a circular sectoral waveguide. The

dyadic Green's function for a hollow circular waveguide was obtained via vector wave functions by Tai[7]. I derive a Fourier-Bessel series representation of the Green's function of a circular sectoral waveguide via scalar potentials.

Solutions based on domain truncation are only valid in certain frequency regimes. In the dynamic case, truncating the domain in the radial direction creates artificial reflections at the truncation boundary. However, the quasi-static excitation employed here evanesces away from the coil which means that the fields are essentially limited to a finite region and may be accurately represented by a discrete basis. The series solution obtained by truncating an infinite domain is the primary advantage of the 'truncated eigenfunction expansion' (TREE) method[8]. The TREE method has been used to solve a number of eddy-current problems. Sun *et al.*[9] found the eddy currents induced in a finite length layered rod by a coaxial coil. Li *et al.*[10] used the TREE method to study pulsed eddy-current systems. Theodoulidis and Bowler[11] have applied the TREE technique to analyze the interaction between an eddy-current coil and a penetrable right-angled conductive wedge.

This chapter proceeds as follows. In Section 2.2 I introduce the scalar decomposition. In Section 2.3 I derive transverse electric (TE) Green's functions for the hollow circular and circular sectoral waveguides. The potential due to a current loop in a circular sectoral waveguide is obtained in Section 2.4. In Section 2.5, the potential due to a circular coil in a circular sectoral waveguide is determined. I arrive at an expression for the impedance of the coil in Section 2.6. Results for a number of wedge geometries are discussed in Section 2.7.

2.2 Scalar Decomposition

For a preferred direction along the z-axis, the frequency-domain electric and magnetic fields may be written in terms of transverse magnetic (TM) and transverse electric (TE) scalar potentials thus[1]

$$\mathbf{E} = \nabla \times \nabla \times [\hat{\mathbf{z}}\psi] - \jmath\omega\mu\nabla \times [\hat{\mathbf{z}}\varphi] \tag{2.1}$$

$$\mathbf{H} = \jmath\omega\epsilon\nabla \times [\hat{\mathbf{z}}\psi] + \nabla \times \nabla \times [\hat{\mathbf{z}}\varphi]. \tag{2.2}$$

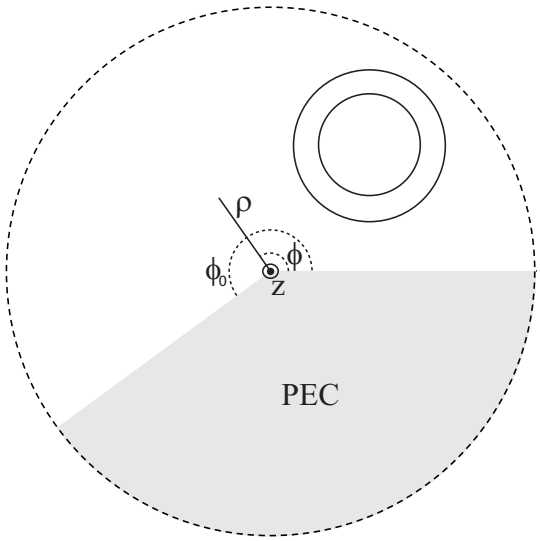

Figure 2.1 Finite eddy-current coil in the presence of an infinite perfectly conducting wedge.

Here ϵ, μ are respectively the permittivity and permeability of the medium. I seek a solution for the potentials ψ and φ due to an eddy-current coil whose axis is in the z-direction, Figure 2.1. The components of the electric and magnetic fields tangential to the wedge surfaces are

$$E_z = \left(\frac{\partial^2}{\partial z^2} + k^2\right)\psi \tag{2.3}$$

$$E_\rho = \frac{\partial^2 \psi}{\partial \rho \partial z} - \jmath\omega\mu\frac{1}{\rho}\frac{\partial \varphi}{\partial \phi} \tag{2.4}$$

$$H_z = \left(\frac{\partial^2}{\partial z^2} + k^2\right)\varphi \tag{2.5}$$

$$H_\rho = \jmath\omega\epsilon\frac{1}{\rho}\frac{\partial \psi}{\partial \phi} + \frac{\partial^2 \varphi}{\partial \rho \partial z}. \tag{2.6}$$

The tangential electric field must vanish on the surfaces of the wedge at $\phi = 0_+$ and $\phi = \phi_{0-}$. Therefore, from (2.3), the TM potential ψ satisfies a Dirichlet boundary condition on the surface of the wedge. Hence, from (2.4), the TE potential φ satisfies a Neumann boundary condition on the surface of the wedge.

The strategy for finding the potentials is as follows. As the axis of the coil is along the z-direction, I assume there is no z-component of the electric field and therefore $\psi = 0$ everywhere. In the absence of the TM potential, the transverse electric potential φ is sufficient to satisfy Maxwell's equations and the Neumann boundary condition on the surface of the wedge. First,

I derive a series representation of the potential due to a TE dipole in the presence of the wedge in a radially truncated domain. For completeness, the TM Green's functions for both the hollow circular and circular sectoral waveguides are included in Appendix A. Next I must find the potential due to a filamentary current loop in the presence of the wedge. To do so I take advantage of an equivalence principle[12] stating that the field due to a filamentary current is the same as that of an infinitesimally thin magnetic shell bounded by the filament. The potential due to a circular loop is found by taking the shell to be a circular disc. Once the loop potential is known, one arrives at the potential due to the coil by integrating over its cross-section.

2.3 Fourier-Bessel Series Representation of the TE Green's Functions

In this section, I propose a Fourier-Bessel series representation of the TE Green's function for the hollow circular and circular sectoral waveguides. I begin with the analysis of the hollow circular waveguide.

2.3.1 Hollow Circular Waveguide

I seek a solution to

$$(\nabla^2 + k^2)g^{(te)}(\rho, \rho_s, \phi - \phi_s, z - z_s) = -\delta(\rho - \rho_s)\delta(\phi - \phi_s)\delta(z - z_s)/\rho \tag{2.7}$$

where $\partial g^{(te)}(a, \rho_s, \phi - \phi_s, z - z_s)/\partial\rho = 0$. An integral representation of the circular waveguide is possible using the incident and scattered field approach. In order to avoid numerical integration I choose to solve the governing equation directly following the Ohm-Rayleigh method [7]. The following standard completeness relations are used in (2.7):

$$\delta(\phi - \phi_s) = \frac{1}{2\pi} \sum_{m=-\infty}^{\infty} \exp[-\jmath m(\phi - \phi_s)] \tag{2.8}$$

and

$$\delta(z - z_s) = \frac{1}{2\pi} \int_{-\infty}^{\infty} \exp[\jmath\beta(z - z_s)]d\beta. \tag{2.9}$$

In this case, I also take advantage of the completeness relation for Bessel functions [2]:

$$\frac{\delta(\rho-\rho_s)}{\rho_s}=\sum_{i=1}^{\infty}\frac{1}{c_{mi}^2}\mathrm{J}_m(\alpha_{mi}\rho)\mathrm{J}_m(\alpha_{mi}\rho_s) \tag{2.10}$$

where $\alpha_{mi}=q_{mi}/a$ where q_{mi} is the ith zero of the derivative of the Bessel function of order m. Also [13]

$$c_{mi}^2=\int_0^a \mathrm{J}_m^2(\alpha_{mi}\rho)\rho d\rho=-\frac{a^2}{2}\mathrm{J}_m(\alpha_{mi}a)\mathrm{J}_m''(\alpha_{mi}a). \tag{2.11}$$

The Green's function may be expanded in a Fourier series in the azimuthal direction

$$g^{(te)}(\rho,\rho_s,\phi-\phi_s,z-z_s)=\sum_{m=-\infty}^{\infty} g_m^{(te)}(\rho,\rho_s,z-z_s)\exp[-\jmath m(\phi-\phi_s)]. \tag{2.12}$$

The unknown coefficients are written as an inverse Fourier transform thus

$$g_m^{(te)}(\rho,\rho_s,z-z_s)=\frac{1}{2\pi}\int_{-\infty}^{\infty}\widetilde{g}_m^{(te)}(\rho,\rho_s)\exp[\jmath\beta(z-z_s)]d\beta. \tag{2.13}$$

By completeness, the radial function may be further expanded in terms of eigenfunctions

$$\widetilde{g}_m^{(te)}(\rho,\rho_s)=\sum_{i=1}^{\infty}A_{mi}(\beta)\frac{1}{c_{mi}^2}\mathrm{J}_m(\alpha_{mi}\rho)\mathrm{J}_m(\alpha_{mi}\rho_s). \tag{2.14}$$

Substituting (2.12), (2.13), and (2.14) in (2.7) yields

$$\begin{aligned}&\left\{\mathcal{L}^2-\gamma^2\right\}\sum_{i=1}^{\infty}A_{mi}(\beta)\frac{1}{c_{mi}^2}\mathrm{J}_m(\alpha_{mi}\rho)\mathrm{J}_m(\alpha_{mi}\rho_s)=\\&\frac{1}{2\pi}\sum_{i=1}^{\infty}\frac{1}{c_{mi}^2}\mathrm{J}_m(\alpha_{mi}\rho)\mathrm{J}_m(\alpha_{mi}\rho_s)\end{aligned} \tag{2.15}$$

where

$$\mathcal{L}^2=-\frac{1}{\rho}\frac{\partial}{\partial\rho}\left(\rho\frac{\partial}{\partial\rho}\right)+\frac{m^2}{\rho^2} \tag{2.16}$$

and $\gamma^2+\beta^2=k^2$. By definition of an eigenfunction,

$$\mathcal{L}^2\mathrm{J}_m(\alpha_{mi}\rho)=\alpha_{mi}^2\mathrm{J}_m(\alpha_{mi}\rho). \tag{2.17}$$

Using (2.17) in (2.15)

$$\begin{aligned}&\sum_{i=1}^{\infty}A_{mi}(\beta)\frac{\alpha_{mi}^2-\gamma^2}{c_{mi}^2}\mathrm{J}_m(\alpha_{mi}\rho)\mathrm{J}_m(\alpha_{mi}\rho_s)=\\&\frac{1}{2\pi}\sum_{i=1}^{\infty}\frac{1}{c_{mi}^2}\mathrm{J}_m(\alpha_{mi}\rho)\mathrm{J}_m(\alpha_{mi}\rho_s).\end{aligned} \tag{2.18}$$

The orthogonality of the Bessel function implies that

$$A_{mi}(\beta) = \frac{1}{2\pi}\frac{1}{\alpha_{mi}^2 - \gamma^2}. \tag{2.19}$$

Therefore, the Green's function for the hollow circular waveguide takes the form

$$\begin{aligned} g^{(te)}(\rho, \rho_s, \phi - \phi_s, z - z_s) = \frac{1}{(2\pi)^2} \sum_{m=-\infty}^{\infty} \exp[-\jmath m(\phi - \phi_s)] \sum_{i=1}^{\infty} \frac{1}{c_{mi}^2} \mathrm{J}_m(\alpha_{mi}\rho_s) \cdot \\ \int_{-\infty}^{\infty} \frac{\mathrm{J}_m(\alpha_{mi}\rho)}{\alpha_{mi}^2 - \gamma^2} \exp[\jmath\beta(z - z_s)] d\beta. \end{aligned} \tag{2.20}$$

Using the definition of γ, equation (2.20) may be expressed as

$$\begin{aligned} g^{(te)}(\rho, \rho_s, \phi - \phi_s, z - z_s) = \frac{1}{(2\pi)^2} \sum_{m=-\infty}^{\infty} \exp[-\jmath m(\phi - \phi_s)] \sum_{i=1}^{\infty} \frac{1}{c_{mi}^2} \mathrm{J}_m(\alpha_{mi}\rho_s) \cdot \\ \int_{-\infty}^{\infty} \frac{\mathrm{J}_m(\alpha_{mi}\rho)}{\alpha_{mi}^2 - k^2 + \beta^2} \exp[\jmath\beta(z - z_s)] d\beta. \end{aligned} \tag{2.21}$$

The denominator of the integrand may be factored thus

$$\begin{aligned} g^{(te)}(\rho, \rho_s, \phi - \phi_s, z - z_s) = \frac{1}{(2\pi)^2} \sum_{m=-\infty}^{\infty} \exp[-\jmath m(\phi - \phi_s)] \sum_{i=1}^{\infty} \frac{1}{c_{mi}^2} \mathrm{J}_m(\alpha_{mi}\rho_s) \cdot \\ \int_{-\infty}^{\infty} \frac{\mathrm{J}_m(\alpha_{mi}\rho) \exp[\jmath\beta(z - z_s)]}{\left(\beta - \sqrt{k^2 - \alpha_{mi}^2}\right)\left(\beta + \sqrt{k^2 - \alpha_{mi}^2}\right)} d\beta. \end{aligned} \tag{2.22}$$

As no branch cut occurs in the integrand of (2.22), the integral may be evaluated via the residue theorem [14]

$$\begin{aligned} g^{(te)}(\rho, \rho_s, \phi - \phi_s, z - z_s) = \sum_{m=-\infty}^{\infty} \exp[-\jmath m(\phi - \phi_s)] \sum_{i=1}^{\infty} \frac{u_{mi}}{c_{mi}^2} \mathrm{J}_m(\alpha_{mi}\rho) \mathrm{J}_m(\alpha_{mi}\rho_s) \cdot \\ \frac{\exp\left[\jmath\sqrt{k^2 - \alpha_{mi}^2}(z - z_s)\right]}{\sqrt{k^2 - \alpha_{mi}^2}} \end{aligned} \tag{2.23}$$

where

$$u_{mi} = \begin{cases} \frac{\jmath}{8\pi} & \alpha_{mi} < k \\ \\ \frac{\jmath}{4\pi} & \alpha_{mi} > k. \end{cases} \tag{2.24}$$

The above assumes that the wavenumber k is real.

2.3.2 Circular sectoral waveguide

The derivation for the circular sectoral waveguide is similar to that of the previous section. The direct Ohm-Raleigh method obviates the need for an integral representation of the Green's function. The governing equation is again

$$(\nabla^2 + k^2)G^{(te)}(\rho, \rho_s, \phi - \phi_s, z - z_s) = -\delta(\rho - \rho_s)\delta(\phi - \phi_s)\delta(z - z_s)/\rho. \tag{2.25}$$

I have Neumann boundary conditions on the surface of the wedge $\partial G^{(te)}(\rho, \rho_s, 0 - \phi_s, z - z_s)/\partial\phi = \partial G^{(te)}(\rho, \rho_s, \phi_0 - \phi_s, z - z_s)/\partial\phi = 0$ and on the walls of the guide $\partial G^{(te)}(a, \rho_s, \phi - \phi_s, z - z_s)/\partial\rho = 0$. Again, I choose to solve (2.25) directly. To this end, I propose the following Eigenfunction expansion of the Green's function

$$\begin{aligned} G^{(te)}(\rho, \rho_s, \phi - \phi_s, z - z_s) = \frac{1}{\phi_0\pi}\sum_{m=0}^{\infty}\sum_{i=1}^{\infty}\frac{1}{c_{mi}^2}\mathrm{J}_\mu(\alpha_{mi}\rho_s)\cos(\mu\phi)\cos(\mu\phi_s)\cdot \\ \int_{-\infty}^{\infty}\frac{\mathrm{J}_\mu(\alpha_{mi}\rho)}{\alpha_{mi}^2 - \gamma^2}\exp[\jmath\beta(z - z_s)]d\beta. \end{aligned} \tag{2.26}$$

Here $\alpha_{mi} = q_{\mu i}/a$ where $q_{\mu i}$ is the ith zero of the derivative of the Bessel function of order $\mu = m\pi/\phi_0$ and

$$c_{mi}^2 = \int_0^a \mathrm{J}_\mu^2(\alpha_{mi}\rho)\rho d\rho = \frac{a^2}{2}\left[\mathrm{J}_\mu^2(\alpha_{mi}a) - \mathrm{J}_{\mu+1}(\alpha_{mi}a)\mathrm{J}_{\mu-1}(\alpha_{mi}a)\right]. \tag{2.27}$$

In order to satisfy the Neumann boundary condition on the surface of the wedge, a Cosine basis is chosen in the azimuthal direction. Again, the integrand in (2.26) may be factored

$$\begin{aligned} G^{(te)}(\rho, \rho_s, \phi - \phi_s, z - z_s) = \frac{1}{\phi_0\pi}\sum_{m=0}^{\infty}\sum_{i=1}^{\infty}\frac{1}{c_{mi}^2}\mathrm{J}_\mu(\alpha_{mi}\rho_s)\cos(\mu\phi)\cos(\mu\phi_s)\cdot \\ \int_{-\infty}^{\infty}\frac{\mathrm{J}_\mu(\alpha_{mi}\rho)\exp[\jmath\beta(z - z_s)]}{\left(\beta - \sqrt{k^2 - \alpha_{mi}^2}\right)\left(\beta + \sqrt{k^2 - \alpha_{mi}^2}\right)}d\beta. \end{aligned} \tag{2.28}$$

The residue theorem implies that

$$\begin{aligned} G^{(te)}(\rho, \rho_s, \phi - \phi_s, z - z_s) = \sum_{m=0}^{\infty}\sum_{i=1}^{\infty}\frac{d_{mi}}{c_{mi}^2}\mathrm{J}_\mu(\alpha_{mi}\rho)\mathrm{J}_\mu(\alpha_{mi}\rho_s)\cos(\mu\phi)\cos(\mu\phi_s)\cdot \\ \frac{\exp\left[\jmath\sqrt{k^2 - \alpha_{mi}^2}(z - z_s)\right]}{\sqrt{k^2 - \alpha_{mi}^2}} \end{aligned} \tag{2.29}$$

where if $m > 0$

$$d_{mi} = \begin{cases} \frac{\jmath}{2\phi_0} & \alpha_{mi} < k \\ \frac{\jmath}{\phi_0} & \alpha_{mi} > k. \end{cases} \tag{2.30}$$

If $m = 0$, the normalization is given by

$$d_{0i} = \begin{cases} \frac{\jmath}{4\phi_0} & \alpha_{0i} < k \\ \frac{\jmath}{2\phi_0} & \alpha_{0i} > k. \end{cases} \tag{2.31}$$

2.4 Potential due to a current-loop inside a circular sectoral waveguide

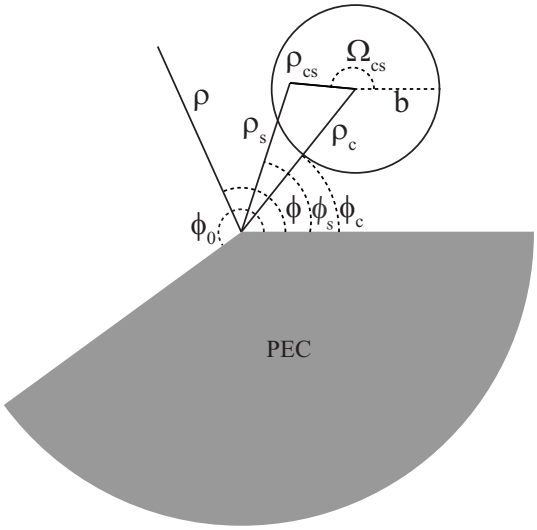

Figure 2.2 Loop Geometry

In this section I consider the total potential due to a current-loop of radius b radiating inside a circular sectoral waveguide, Figure 2.2. The potential due to the loop source may be derived from the TE Green's function of Section 2.3

$$G^{(te)}(\rho, \rho_s, \phi - \phi_s, z - z_s) = \sum_{m=0}^{\infty} \sum_{i=1}^{\infty} \frac{d_{mi}}{c_{mi}^2} \mathrm{J}_\mu(\alpha_{mi}\rho) \mathrm{J}_\mu(\alpha_{mi}\rho_s) \cos(\mu\phi) \cos(\mu\phi_s) \cdot \frac{\exp\left[-\jmath\sqrt{k^2 - \alpha_{mi}^2}(z - z_s)\right]}{\sqrt{k^2 - \alpha_{mi}^2}}. \tag{2.32}$$

The first step is to use the addition theorem to establish a new coordinate system at the center of the loop. Graf's addition theorem may be used to shift the expansion to the center of the

loop[15]

$$\mathrm{J}_{\mu}(\alpha_{mi}\rho_s)\cos(\mu\phi_s) = \sum_{v=-\infty}^{\infty} \mathrm{J}_{v}(\alpha_{mi}\rho_{cs})\mathrm{J}_{\mu-v}(\alpha_{mi}\rho_c)\cdot \\ \{\cos[(\mu-v)(-\phi_c)]\cos(v\Omega_{cs}) + \sin[(\mu-v)(-\phi_c)]\sin(v\Omega_{cs})\}\,. \tag{2.33}$$

I are free to substitute (2.33) into (2.32)

$$G^{(te)}(\rho,\rho_c,\phi,\phi_c,z-z_s) = \sum_{m=0}^{\infty}\sum_{i=1}^{\infty}\frac{d_{mi}}{c_{mi}^2}\mathrm{J}_{\mu}(\alpha_{mi}\rho)\cos(\mu\phi)\frac{\exp\left[-\jmath\sqrt{k^2-\alpha_{mi}^2}(z-z_s)\right]}{\sqrt{k^2-\alpha_{mi}^2}}\cdot \\ \sum_{v=-\infty}^{\infty}\mathrm{J}_{v}(\alpha_{mi}\rho_{cs})\mathrm{J}_{\mu-v}(\alpha_{mi}\rho_c)\cdot \\ \{\cos[(\mu-v)(-\phi_c)]\cos(v\Omega_{cs}) + \sin[(\mu-v)(-\phi_c)]\sin(v\Omega_{cs})\}\,. \tag{2.34}$$

Per the magnetic shell model, the potential due to the loop current is obtained by integrating (2.34) over a disc of radius b centered on ρ_c

$$\varphi_L(\rho,\rho_c,\phi,\phi_c,z-z_s) = \\ \int_0^{2\pi} d\Omega_{cs}\int_0^{b} d\rho_{cs}\rho_{cs}G^{(te)}(\rho,\rho_c,\phi,\phi_c,z-z_s) = \\ \sum_{m=0}^{\infty}\sum_{i=1}^{\infty}\frac{d_{mi}}{c_{mi}^2}\mathrm{J}_{\mu}(\alpha_{mi}\rho)\cos(\mu\phi)\frac{\exp\left[-\jmath\sqrt{k^2-\alpha_{mi}^2}(z-z_s)\right]}{\sqrt{k^2-\alpha_{mi}^2}}\cdot \\ \sum_{v=-\infty}^{\infty}\mathrm{J}_{\mu-v}(\alpha_{mi}\rho_c)\int_0^{b} d\rho_{cs}\rho_{cs}\mathrm{J}_{v}(\alpha_{mi}\rho_{cs})\cdot \\ \left\{\cos[(\mu-v)(-\phi_c)]\int_0^{2\pi} d\Omega_{cs}\cos(v\Omega_{cs}) + \sin[(\mu-v)(-\phi_c)]\int_0^{2\pi} d\Omega_{cs}\sin(v\Omega_{cs})\right\}. \tag{2.35}$$

Only the $v=0$ term remains after the integral over Ω_{cs} is carried out

$$\varphi_L(\rho,\rho_c,\phi,\phi_c,z-z_s) = \\ 2\pi\sum_{m=0}^{\infty}\sum_{i=1}^{\infty}\frac{d_{mi}}{c_{mi}^2}\mathrm{J}_{\mu}(\alpha_{mi}\rho)\cos(\mu\phi)\frac{\exp\left[-\jmath\sqrt{k^2-\alpha_{mi}^2}(z-z_s)\right]}{\sqrt{k^2-\alpha_{mi}^2}}\cdot \\ \mathrm{J}_{\mu}(\alpha_{mi}\rho_c)\cos(\mu\phi_c)\int_0^{b} d\rho_{cs}\rho_{cs}\mathrm{J}_0(\alpha_{mi}\rho_{cs}). \tag{2.36}$$

The integral over ρ_{cs} may be evaluated analytically ([16], 5.56(2))

$$\begin{aligned}&\varphi_L(\rho,\rho_c,\phi,\phi_c,z-z_s)=\\&2\pi\sum_{m=0}^{\infty}\sum_{i=1}^{\infty}\frac{d_{mi}}{c_{mi}^2}\mathrm{J}_\mu(\alpha_{mi}\rho)\cos(\mu\phi)\frac{\exp\left[-\jmath\sqrt{k^2-\alpha_{mi}^2}(z-z_s)\right]}{\sqrt{k^2-\alpha_{mi}^2}}\cdot\\&\mathrm{J}_\mu(\alpha_{mi}\rho_c)\cos(\mu\phi_c)\frac{b\mathrm{J}_1(\alpha_{mi}b)}{\alpha_{mi}}.\end{aligned}\tag{2.37}$$

2.5 Potential due to a circular coil inside a circular sectoral waveguide

The potential due to a circular coil of N turns may be derived from the expression for the loop-potential (2.37) by superposition. I integrate (2.37) over the the loop radius b from the inner radius of the coil r_1 to the outer radius r_2. Similarly, the loop potential is integrated over the source point z_s from the lower surface of the coil z_1 to the upper surface z_2

$$\begin{aligned}&\varphi_C(\rho,\rho_c,\phi,\phi_c,z)=\\&2\pi\nu\sum_{m=0}^{\infty}\sum_{i=1}^{\infty}\frac{d_{mi}}{c_{mi}^2\beta_{mi}}\mathrm{J}_\mu(\alpha_{mi}\rho)\cos(\mu\phi)\mathrm{Q}_{mi}(z,z_1,z_2)\cdot\\&\mathrm{J}_\mu(\alpha_{mi}\rho_c)\cos(\mu\phi_c)\int_{r_1}^{r_2}db\frac{b\mathrm{J}_1(\alpha_{mi}b)}{\alpha_{mi}}\end{aligned}\tag{2.38}$$

where the turns density $\nu=N/[(z_2-z_1)(r_2-r_1)]$,

$$\mathrm{Q}_{mi}(z,z_1,z_2)=\begin{cases}\left\{\exp[\jmath\beta_{mi}(z_2-z)]-\exp[-\jmath\beta_{mi}(z-z_1)]\right\}/\jmath\beta_{mi} & z\geq z_2\\ \left\{2-\exp[-\jmath\beta_{mi}(z-z_1)]-\exp[\jmath\beta_{mi}(z-z_2)]\right\}/\jmath\beta_{mi} & z_1\leq z\leq z_2\\ \left\{\exp[\jmath\beta_{mi}(z-z_1)]-\exp[\jmath\beta_{mi}(z-z_2)]\right\}/\jmath\beta_{mi} & z\leq z_1\end{cases}\tag{2.39}$$

and $\beta_{mi}=\sqrt{k^2-\alpha_{mi}^2}$. The integral in (2.38) may be computed analytically ([16], 6.561(1))

$$\begin{aligned}&\varphi_C(\rho,\rho_c,\phi,\phi_c,z)=\\&2\pi\nu\sum_{m=0}^{\infty}\sum_{i=1}^{\infty}\frac{d_{mi}}{c_{mi}^2\beta_{mi}}\mathrm{J}_\mu(\alpha_{mi}\rho)\cos(\mu\phi)\mathrm{Q}_{mi}(z,z_1,z_2)\cdot\\&\mathrm{J}_\mu(\alpha_{mi}\rho_c)\cos(\mu\phi_c)\chi_{mi}(r_2,r_1)\end{aligned}\tag{2.40}$$

where

$$\chi_{mi}(r_2,r_1)=\frac{1}{6}\left[{}_1\mathrm{F}_2\left(\frac{3}{2};2,\frac{5}{2};-\frac{1}{4}\alpha_{mi}^2r_2^2\right)r_2^3-{}_1\mathrm{F}_2\left(\frac{3}{2};2,\frac{5}{2};-\frac{1}{4}\alpha_{mi}^2r_1^2\right)r_1^3\right].\tag{2.41}$$

Here ${}_1\mathrm{F}_2$ is the generalized hypergeometric function.

2.6 Impedance

Next I calculate the impedance of the coil in the presence of a conducting wedge. I must calculate the flux linked by the coil. First I apply Graf's addition theorem to (2.40)

$$\begin{aligned}
&\varphi_C(\rho,\rho_c,\phi,\phi_c,z) = \\
&2\pi\nu\sum_{m=0}^{\infty}\sum_{i=1}^{\infty}\frac{d_{mi}}{c_{mi}^2\beta_{mi}}\sum_{v=-\infty}^{\infty}\mathrm{J}_v(\alpha_{mi}\rho_{co})\mathrm{J}_{\mu-v}(\alpha_{mi}\rho_c)\cdot \\
&\{\cos[(\mu-v)(-\phi_c)]\cos(v\Omega_{co})+\sin[(\mu-v)(-\phi_c)]\sin(v\Omega_{co})\}\,\mathrm{Q}_{mi}(z,z_1,z_2)\cdot \\
&\mathrm{J}_\mu(\alpha_{mi}\rho_c)\cos(\mu\phi_c)\chi_{mi}(r_2,r_1)
\end{aligned} \tag{2.42}$$

The flux linked by a single circular filament of radius r_0 at $z = z_0$ may be calculated by integrating the z-component of the magnetic flux density

$$\begin{aligned}
&\Phi_L(\rho_c,\phi_c) = \\
&2\pi\mu_0\nu\sum_{m=0}^{\infty}\sum_{i=1}^{\infty}\frac{d_{mi}}{c_{mi}^2\beta_{mi}}\sum_{v=-\infty}^{\infty}\alpha_{mi}^2\int_0^{2\pi}d\Omega_{co}\int_0^{r_0}d\rho_{co}\rho_{co}\mathrm{J}_v(\alpha_{mi}\rho_{co})\mathrm{J}_{\mu-v}(\alpha_{mi}\rho_c)\cdot \\
&\{\cos[(\mu-v)(-\phi_c)]\cos(v\Omega_{co})+\sin[(\mu-v)(-\phi_c)]\sin(v\Omega_{co})\}\,\mathrm{Q}_{mi}(z_0,z_1,z_2)\cdot \\
&\mathrm{J}_\mu(\alpha_{mi}\rho_c)\cos(\mu\phi_c)\chi_{mi}(r_2,r_1)
\end{aligned} \tag{2.43}$$

Again, only the $v = 0$ survives the integration over Ω_{co}

$$\begin{aligned}
&\Phi_L(\rho_c,\phi_c) = \\
&(2\pi)^2\mu_0\nu\sum_{m=0}^{\infty}\sum_{i=1}^{\infty}\frac{d_{mi}}{c_{mi}^2\beta_{mi}}\alpha_{mi}^2\mathrm{J}_\mu(\alpha_{mi}\rho_c)\cos[(\mu)(-\phi_c)]\cdot \\
&\mathrm{J}_\mu(\alpha_{mi}\rho_c)\cos(\mu\phi_c)\chi_{mi}(r_2,r_1)\mathrm{Q}_{mi}(z_0,z_1,z_2)\int_0^{r_0}d\rho_{co}\rho_{co}\mathrm{J}_0(\alpha_{mi}\rho_{co}).
\end{aligned} \tag{2.44}$$

Evaluating the integral over ρ_{co} analytically yields

$$\begin{aligned}
&\Phi_L(\rho_c,\phi_c) = \\
&(2\pi)^2\mu_0\nu\sum_{m=0}^{\infty}\sum_{i=1}^{\infty}\frac{d_{mi}}{c_{mi}^2\beta_{mi}}\alpha_{mi}^2\mathrm{J}_\mu^2(\alpha_{mi}\rho_c)\cos^2(\mu\phi_c)\chi_{mi}(r_2,r_1)\cdot \\
&\frac{r_0\mathrm{J}_1(\alpha_{mi}r_0)}{\alpha_{mi}}\mathrm{Q}_{mi}(z_0,z_1,z_2).
\end{aligned} \tag{2.45}$$

The total flux may be obtained by integrating (2.45) over the cross section of the coil

$$\begin{aligned}&\Phi_C(\rho_c,\phi_c)=\\&(2\pi)^2\mu_0\nu^2\sum_{m=0}^{\infty}\sum_{i=1}^{\infty}\frac{d_{mi}}{c_{mi}^2\beta_{mi}}\alpha_{mi}^2\mathrm{J}_\mu^2(\alpha_{mi}\rho_c)\cos^2(\mu\phi_c)\chi_{mi}(r_2,r_1)\cdot\\&\int_{r_1}^{r_2}dr_0\frac{r_0\mathrm{J}_1(\alpha_{mi}r_0)}{\alpha_{mi}}\int_{z_1}^{z_2}dz_0\mathrm{Q}_{mi}(z_0,z_1,z_2).\end{aligned}\tag{2.46}$$

The integral over z may be evaluated based on the definition of $\mathrm{Q}_{mi}(z,z_1,z_2)$

$$\begin{aligned}&\Phi_C(\rho_c,\phi_c)=\\&(2\pi)^2\mu_0\nu^2\sum_{m=0}^{\infty}\sum_{i=1}^{\infty}\frac{d_{mi}}{c_{mi}^2}\frac{\alpha_{mi}^2}{\beta_{mi}}\mathrm{J}_\mu^2(\alpha_{mi}\rho_c)\cos^2(\mu\phi_c)\chi_{mi}^2(r_2,r_1)\cdot\\&\left(\frac{2(z_2-z_1)}{\jmath\beta_{mi}}+\frac{2}{\beta_{mi}^2}\left\{1-\exp[\jmath\beta_{mi}(z_1-z_2)]\right\}\right).\end{aligned}\tag{2.47}$$

The induced emf is related to the flux by a time derivative

$$\begin{aligned}&V_C(\rho_c,\phi_c)=IZ_C(\rho_c,\phi_c)=\\&-\jmath\omega I(2\pi)^2\mu_0\nu^2\sum_{m=0}^{\infty}\sum_{i=1}^{\infty}\frac{d_{mi}}{c_{mi}^2}\frac{\alpha_{mi}^2}{\beta_{mi}}\mathrm{J}_\mu^2(\alpha_{mi}\rho_c)\cos^2(\mu\phi_c)\chi_{mi}^2(r_2,r_1)\cdot\\&\left(\frac{2(z_2-z_1)}{\jmath\beta_{mi}}+\frac{2}{\beta_{mi}^2}\left\{1-\exp[\jmath\beta_{mi}(z_1-z_2)]\right\}\right).\end{aligned}\tag{2.48}$$

Finally, the impedance is given by

$$\begin{aligned}&Z_C(\rho_c,\phi_c)=\\&-\jmath\omega(2\pi)^2\mu_0\nu^2\sum_{m=0}^{\infty}\sum_{i=1}^{\infty}\frac{d_{mi}}{c_{mi}^2}\frac{\alpha_{mi}^2}{\beta_{mi}}\mathrm{J}_\mu^2(\alpha_{mi}\rho_c)\cos^2(\mu\phi_c)\chi_{mi}^2(r_2,r_1)\mathrm{U}_{mi}(z_1,z_2)\end{aligned}\tag{2.49}$$

where

$$\mathrm{U}_{mi}(z_1,z_2)=\left(\frac{2(z_2-z_1)}{\jmath\beta_{mi}}+\frac{2}{\beta_{mi}^2}\left\{1-\exp[\jmath\beta_{mi}(z_1-z_2)]\right\}\right).\tag{2.50}$$

2.7 Results and Validation

2.7.1 Validation

Validation of the TREE method presented in this chapter was accomplished in the following way. When the wedge angle ϕ_0 is set equal to π, the geometry reduces to a tangent coil over a PEC half-space. My theory was compared to an integral expression for the impedance change

of a horizontal coil over a conducting half-space derived by Burke[17] (See Figure 2.3). One observes excellent agreement over a range of distances from the conductor (lift-off).

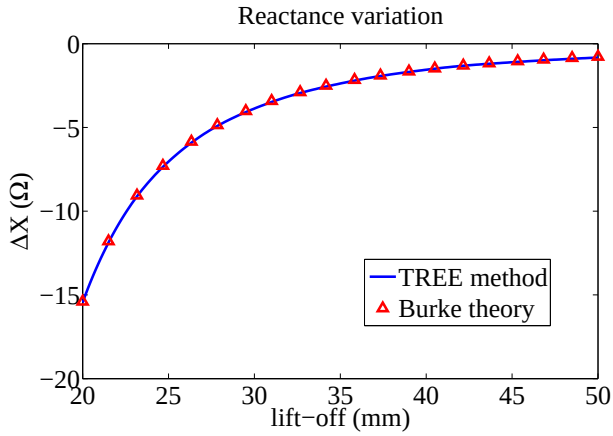

Figure 2.3 Theoretical reactance change as a function of coil lift-off using TREE method (blue line) and Burke theory (red triangles).

2.7.2 Results for wedge angles of 225 and 270 degrees

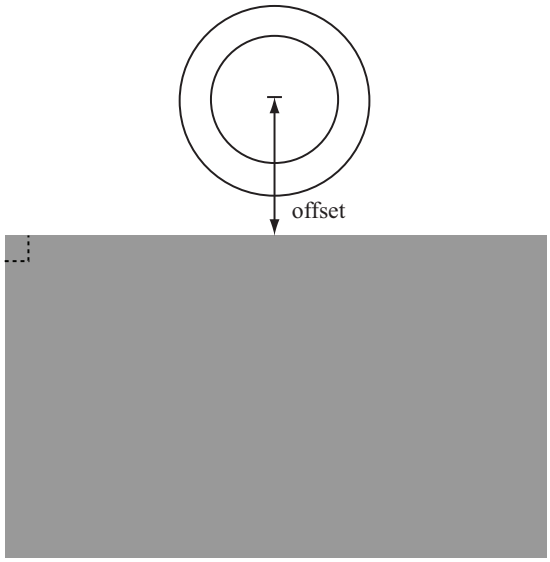

Figure 2.4 Quarter-space Geometry.

A number of wedge geometries were studied. First consider a coil above a quarter-space conductor (Figure 2.4). The excitation is provided by coil C5 at 850 Hz. In order to compute

the impedance of the coil, equation (2.49) was implemented in MATLAB. The domain was truncated at a radius $a = 200$ mm. The summation over the azimuthal harmonics was limited to 45 terms. For each azimuthal basis function, 40 zeros were included in the summation. The change in impedance of the coil is shown in Figure 2.5. The conductor is in the right half-space where the coil position is positive. Away from the conductor (negative coil position), the impedance is nearly unchanged from the free-space self-inductance of the coil. As the coil moves over the edge of the conductor, currents induced on the surface of the metal decrease the flux linked by the coil and the impedance drops. As the coil moves away from the edge, the impedance approaches that of a coil over a half-space conductor.

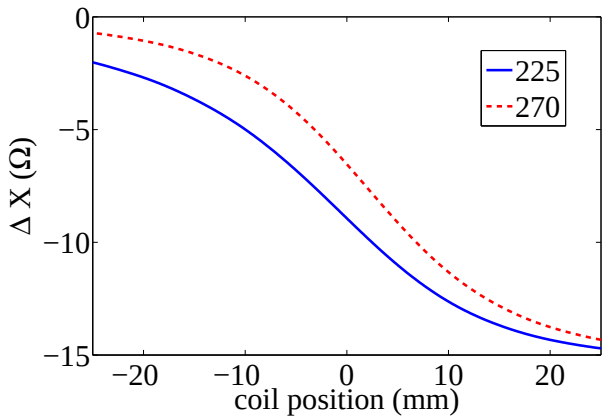

Figure 2.5 Reactance variation with coil axis position relative to the vertex for wedges of angle 225 (solid line) and 270 (dashed line) degrees for coil C5 excited at 850 Hz and a lift-off of 20 mm.

Figure 2.5 also shows the reactance variation for the C5 coil in the presence of a wedge of angle 225 degrees. The coil movement and position is the same as for the quarter-space geometry. I observe that the impedance change is slightly greater at the initial position than for the quarter-space geometry. The wedge is initially closer to the coil for the 225 degree wedge than for the 270 degree wedge. The proximity of the wedge face accounts for the slightly larger $|\Delta X|$. As the coil moves toward the vertex of the wedge the impedance is driven down. The transition is somewhat more gradual due to the smaller wedge angle. Away from the vertex over the wedge the impedance again approaches that of a coil over a perfectly conducting

half-space.

2.7.3 Conducting Sheet

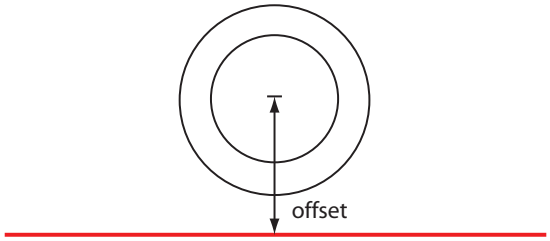

Figure 2.6 Conducting Sheet Geometry.

Next I consider an eddy-current coil interacting with a conducting sheet, Figure 2.6. The wedge reduces to a conducting sheet when the wedge angle ϕ_0 equals 2π. Again, away from the sheet the coil impedance is unchanged from its free-space value. As the coil moves over the sheet the impedance drops in accordance with Lenz's law (Figure 2.7). Here the edge singularity is relatively weak as the field produced by the coil is entirely TE_z. Away from the edge the impedance again approaches that of a coil over a conducting half space.

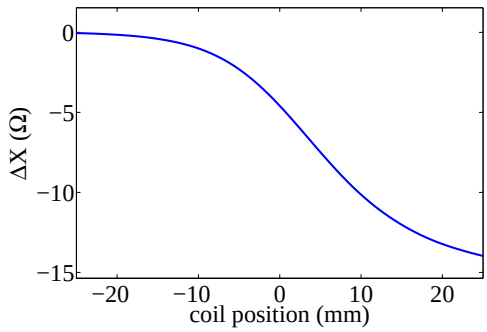

Figure 2.7 Reactance variation with coil axis position relative to the edge of the conducting sheet for coil C5 excited at 850 Hz.

2.8 Conclusion

A closed-form expression for the impedance of an eddy-current coil in the presence of an infinite conducting wedge of arbitrary angle has been derived. The TREE solution given here is valid in the quasi-static frequency regime. My theory was validated via comparison to an expression for the impedance change of a horizontal coil over a conducting half-space. Three geometries were studied: a conducting quarter-space, a conducting wedge of angle 225 degrees, and a semi-infinite conducting sheet. The theory predicts a measurable change in the tangent coil reactance in the presence of all three geometries.

CHAPTER 3 Control of electromagnetic edge effects in electrically-small rectangular plasma reactors

3.1 Literature Review

Plasma enhanced chemical vapor deposition (PECVD) of thin films may be achieved via rectangular parallel plate reactors. In a typical system, a neutral gas is pumped into a vacuum chamber. The gas passes through an RF electrode with a showerhead and is ionized by an electric field to form a plasma. A narrow space charge sheath forms around the plasma near hard surfaces. The material to be deposited is accelerated across the sheath toward the substrate. By-products are pumped out of the chamber to maintain vacuum. Many industrial applications require thin films to be deposited uniformly across the surface of a substrate. Solar cells require layer thicknesses that are uniform to within $\pm 10\%$. Nonuniformity less than $\pm 5\%$ is necessary for thin film transistors for flat screens. However, practical reactor systems exhibit variations in the electric field that lead to non-uniform deposition.

The electromagnetic fields inside the reactor may be decomposed into standing and edge wave components. The standing wave results from the superposition of traveling waves originating from the feed and propagating in opposite directions. Edge waves are evanescent waves that decay from the plasma edge toward the center of the reactor. For large-area reactors, variations in the standing wave across the electrode surface contribute to nonuniformity. The standing wave voltage distribution across the electrode without plasma in the chamber was studied theoretically by Sansonnens *et al.*[18] Voltage uniformity across the electrode was examined as a function of frequency and feed position. Determining the influence of a plasma on the fields in a rectangular reactor is challenging. A numerical quasi-planar (QP) model has been used to study the standing wave in the presence of a plasma.[19] The QP model was used

to calculate an electrode shape that suppressed the standing wave to improve nonuniformity. Chen *et al.* study the effects of an inhomogeneous plasma via full-wave simulations that couple Maxwell's equations to transport equations for charged and neutral particles.[20] The behavior of H_2 plasmas in a reactor of area 3.05×2.85 m^2 is examined over a range of frequencies from 13.56 MHz to 200 MHz.

Analytical studies have concentrated on cylindrical reactors. Lieberman *et al.* leverage mode-matching techniques to study standing wave and skin effects in a cylindrical reactor.[21] In their non-self-consistent approach, the plasma is modeled as a homogeneous slab consisting of a free electron gas. A transmission-line formalism was used to study standing wave and skin effects. Chabert *et al.* study the standing wave in a cylindrical reactor via a self-consistent approach that includes local particle and energy balance in the sheath region.[22] The electromagnetic fields are calculated based on a nonlinear one-dimensional transmission line model. Sansonnens *et al.* study standing wave suppression in a cylindrical reactor without plasma.[23] They demonstrate that a Gaussian electrode shape is optimal for standing wave suppression. Chabert *et al.* confirmed that a Gaussian is the optimal shape with plasma in the chamber.[24] The effect of electrode asymmetry on the fields in a cylindrical reactor has also been analyzed in terms of eigenfunctions.[25] Asymmetric electrodes force the current to redistribute itself along the plasma to ensure current continuity, the so-called telegraph effect. The telegraph effect dominates standing-wave nonuniformity for asymmetric cylindrical reactors at low frequency. Dispersion relations for even and odd standing wave modes have been derived.

While the standing wave is of primary importance for large-area reactors, edge waves dominate nonuniformity for electrically-small reactors. In this chapter, I study the standing and evanescent waves supported by an electrically-small rectangular reactor with plasma in the chamber. Unlike previous quasi-planar approaches, my model includes edge-effects due to the reactor sidewalls. Modal field decompositions are employed under the homogeneous plasma slab approximation. The plasma density remains relatively uniform so long as the dimensions of the reactor remain small with respect to wavelength (less than $\lambda/10$). I determine the amplitude of each mode analytically and show that the field can be represented by the standing

wave, evanescent waves tied to the edges, and an evanescent wave tied to the corners of the reactor. Uniformity may be significantly improved by introducing an impedance boundary condition (IBC) at the plasma edge.

This chapter is organized as follows. In Section 3.2, I introduce the scalar decomposition used to represent the fields. In Section 3.3, I determine the Fourier series coefficients of the standing wave in the sheath and plasma regions. Section 3.4 describes the influence of evanescent waves on the total field. I solve for the evanescent wave coefficients given impedance boundary conditions at the plasma edge. In Section 3.5 I present the results for a number of reactor dimensions. The impact of the impedance boundary condition on uniformity is quantified. Section 3.6 summarizes my results and conclusions.

3.2 Scalar Decomposition

For a preferred direction along the z-axis, the frequency-domain electric and magnetic fields may be expressed in terms of TM (ψ) and TE (φ) scalar potentials[1]

$$\mathbf{E} = \nabla \times \nabla \times [\hat{\mathbf{z}}\psi] - \jmath\omega\mu_p \nabla \times [\hat{\mathbf{z}}\varphi] \tag{3.1}$$

$$\mathbf{H} = \jmath\omega\epsilon_p \nabla \times [\hat{\mathbf{z}}\psi] + \nabla \times \nabla \times [\hat{\mathbf{z}}\varphi] \tag{3.2}$$

where ϵ_p, μ_p are the material parameters in region p. In source-free regions, the potentials satisfy the homogeneous Helmholtz equation

$$\left(\nabla^2 + k_p^2\right)\psi = 0 \tag{3.3}$$

and

$$\left(\nabla^2 + k_p^2\right)\varphi = 0 \tag{3.4}$$

where $k_p^2 = \omega^2\epsilon_p\mu_p$. My strategy for determining the potentials is as follows. The total potential is the superposition of three terms: a standing wave, evanescent edge waves, and an evanescent corner wave. The standing wave is expanded in a Fourier series with unknown coefficients in the sheath and plasma regions. I solve for the unknown coefficients by enforcing boundary conditions along the sheath-vacuum interface at $z = t/2$. The amplitude of the

evanescent edge waves and the corner wave are chosen to satisfy boundary conditions on the reactor sidewalls.

3.3 Standing Wave

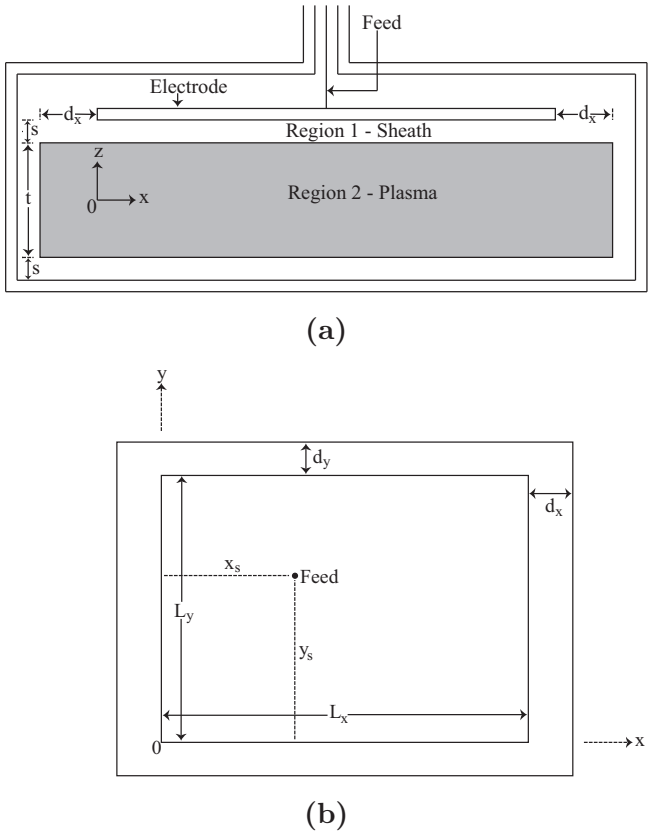

Figure 3.1 Cross-sectional(a) and top(b) view of plasma reactor.

I begin my analysis with the standing wave. Figure 3.1a shows a cross-section of the plasma reactor. The plasma is modeled as a uniform slab surrounded by two vacuum sheaths. Changes in the plasma density caused by field nonuniformities are neglected to permit modal analysis.[25] The unperturbed field is generated by a point current source connected to the back of the top electrode. As the skin depth in aluminum is small at low frequencies, the electrode may be modeled as two current sheets, one for the top surface and one for the bottom surface. Current and voltage continuity are enforced at the edges of the electrode. The incident field

coefficients $A_{mn}^{(0)}$ for this model were determined by Sansonnens *et al.*[18]

$$\psi^{(0)}(x,y) = \sum_{mn} A_{mn}^{(0)} \exp[-\jmath\pi(mx/L_x + ny/L_y)] \tag{3.5}$$

where

$$\begin{aligned} A_{mn}^{(0)} =& 2\jmath\omega\mu_0\{\exp[-\jmath\pi(mx_s/L_x + ny_s/L_y)] \\ &+ \exp[\jmath\pi(mx_s/L_x + ny_s/L_y)]\}/k_1^2\beta_1^2 L_x L_y, \end{aligned}$$

L_x and L_y are the length and width of the electrode, $\beta_1 = \sqrt{k_1^2 - (\pi m/L_x)^2 - (\pi n/L_y)^2}$, $k_1^2 = \omega^2\epsilon_1\mu_1$, and (x_s, y_s) is the location of the source point (Figure 3.1b). In order to facilitate the analysis to come I change to a standing wave basis

$$\begin{aligned} \psi^{(0)}(x,y) =& \sum_{mn} a_{mn}^{(0)} \cos(m\pi x/L_x)\cos(n\pi y/L_y) \\ &+ b_{mn}^{(0)} \cos(m\pi x/L_x)\sin(n\pi y/L_y) \\ &+ c_{mn}^{(0)} \sin(m\pi x/L_x)\cos(n\pi y/L_y) \\ &+ d_{mn}^{(0)} \sin(m\pi x/L_x)\sin(n\pi y/L_y). \end{aligned} \tag{3.6}$$

For this particular excitation, $b_{mn}^{(0)} = c_{mn}^{(0)} = 0$. The TM standing wave in region 1 is a sum of the incident and scattered potentials

$$\begin{aligned} &\psi_1^{(s)}(x,y,z) = \\ &\sum_{m,n\geq 0} a_{mn} \cos(m\pi x/L_x)\cos(n\pi y/L_y)\cos[\beta_1(t/2+s-z)] \\ &+ a_{mn}^{(0)} \cos(m\pi x/L_x)\cos(n\pi y/L_y) \\ &+ \sum_{m,n>0} b_{mn} \sin(m\pi x/L_x)\sin(n\pi y/L_y)\cos[\beta_1(t/2+s-z)] \\ &+ d_{mn}^{(0)} \sin(m\pi x/L_x)\sin(n\pi y/L_y). \end{aligned} \tag{3.7}$$

The TE standing wave in region 1 may also be written as a Fourier series

$$\begin{aligned} &\varphi_1^{(s)}(x,y,z) = \\ &\sum_{m,n\geq 0} c_{mn} \cos(m\pi x/L_x)\cos(n\pi y/L_y)\sin[\beta_1(t/2+s-z)] \\ &+ \sum_{m,n>0} d_{mn} \sin(m\pi x/L_x)\sin(n\pi y/L_y)\sin[\beta_1(t/2+s-z)]. \end{aligned} \tag{3.8}$$

The fields in region 1 satisfy PEC boundary conditions on the surface of the electrode.

The standing wave in the plasma region is similarly decomposed into even and odd modes

$$\begin{aligned}\psi_2^{(s)}(x,y,z) = \\ \sum_{m,n\geq 0} p_{mn}\cos(m\pi x/L_x)\cos(n\pi y/L_y)\cos(\beta_2 z) \\ + \sum_{m,n>0} q_{mn}\sin(m\pi x/L_x)\sin(n\pi y/L_y)\cos(\beta_2 z)\end{aligned} \tag{3.9}$$

$$\begin{aligned}\varphi_2^{(s)}(x,y,z) = \\ \sum_{m,n\geq 0} r_{mn}\cos(m\pi x/L_x)\cos(n\pi y/L_y)\sin(\beta_2 z) \\ + \sum_{m,n>0} s_{mn}\sin(m\pi x/L_x)\sin(n\pi y/L_y)\sin(\beta_2 z)\end{aligned} \tag{3.10}$$

where $\beta_2 = \sqrt{k_2^2 - (\pi m/L_x)^2 - (\pi n/L_y)^2}$, and $k_2^2 = \omega^2\epsilon_2\mu_2$. The TM potential is seen to be even in z. Odd modes present due to the asymmetry of the chamber are neglected.[25] I employ the Drude free electron model[26] for the plasma permittivity

$$\epsilon_{2r} = 1 - \frac{\omega_p^2}{(\omega^2 - \jmath\gamma_p\omega)} \tag{3.11}$$

where γ_p is a damping coefficient and the plasma frequency $\omega_p = 2\pi(8980)\sqrt{n_e}$ depends on the electron number density n_e. For a collisionless plasma the skin depth is given by $\delta = c/\omega_p$ where c is the speed of light.

The unknown coefficients may be found by enforcing the continuity of tangential $\mathbf{E}$ and $\mathbf{H}$ at the plasma-sheath interface at $z = t/2$. Orthogonality of the Fourier series yields two systems of equations that may be expressed in matrix form

$$\mathbf{Z}\mathbf{C_d} = \mathbf{A_0} \tag{3.12}$$

$$\mathbf{Z}\mathbf{C_{vn}} = \mathbf{D_0} \tag{3.13}$$

where $\mathbf{C_d} = \begin{bmatrix} a_{mn} \\ d_{mn} \\ p_{mn} \\ s_{mn} \end{bmatrix}$ and $\mathbf{C_{vn}} = \begin{bmatrix} b_{mn} \\ c_{mn} \\ q_{mn} \\ r_{mn} \end{bmatrix}$ are the vectors of unknown coefficients. The impedance matrix $\mathbf{Z}$ and vectors $\mathbf{A_0}$ and $\mathbf{D_0}$ are defined in Appendix B. The unknown coeffi-

cients are found by inverting the impedance matrix

$$\mathbf{C_d} = \mathbf{Z}^{-1}\mathbf{A_0} \tag{3.14}$$

$$\mathbf{C_{vn}} = \mathbf{Z}^{-1}\mathbf{D_0}. \tag{3.15}$$

Solutions for the scattered standing wave coefficients for practical problems indicate that the magnitude of the scattered standing wave is very small compared to the incident field. This is further theoretical evidence corroborating the claim that the standing wave does not penetrate the plasma. Consequently, the TE scalar potential is neglected for the balance of this chapter.

3.4 Evanescent waves and edge effects

3.4.1 Edge Waves

I have yet to satisfy boundary conditions on the reactor sidewalls ($x = -d_x, L_x + d_x; y = -d_y, L_y + d_y$). The vacuum gap between the plasma and the sidewall is small relative to the reactor dimensions. For electrically-small reactors, field nonuniformity is dominated by the edge waves needed to satisfy by the boundary condition near the plasma edge. However, these edge effects may be ameliorated by introducing an impedance boundary condition on the surface of the sidewall

$$\mathbf{E_{tan}} = Z_c \hat{\mathbf{n}} \times \mathbf{H} \tag{3.16}$$

where Z_c is the impedance and $\hat{\mathbf{n}}$ is a unit vector normal to the surface. Suppose the sidewalls of the reactor box are lined with a layer of lossy material. Then the impedance at the surface of the layer is given by

$$Z_c = \sqrt{\frac{\mu_{cr}\mu_0}{\epsilon_{cr}\epsilon_0}} \tanh(\jmath 2\pi t_c \sqrt{\epsilon_{cr}\mu_{cr}}/\lambda) \tag{3.17}$$

where t_c is the thickness of the layer, and ϵ_{cr} and μ_{cr} are its relative permittivity and permeability, respectively.

Consider the wall near the plasma edge at $x = L_x + d_x$. In between the electrode edge and

the sidewall the potential is composed of waves that evanesce in the x-direction

$$\begin{aligned}
&\psi_1^{(w)}(x,y) = \\
&\sum_{mn} \left\{ a_{mn}^{(r+)} \exp[\beta_n(x-L_x)] + a_{mn}^{(r-)} \exp[-\beta_n(x-L_x)] \right\} \\
&\times \cos(n\pi y/L_y) \\
&+ \left\{ d_{mn}^{(r+)} \exp[\beta_n(x-L_x)] + d_{mn}^{(r-)} \exp[-\beta_n(x-L_x)] \right\} \\
&\times \sin(n\pi y/L_y)
\end{aligned} \tag{3.18}$$

where $\beta_n = \jmath\sqrt{k_2^2 - (n\pi/L_y)^2}$. Imposing the IBC at the sidewall eliminates $a_{mn}^{(r-)}$ and $d_{mn}^{(r-)}$

$$\begin{aligned}
&\psi_1^{(w)}(x,y) = \\
&\sum_{mn} a_{mn}^{(r+)} \left\{ \exp[\beta_n(x-L_x)] + b_{mn}^{(-)} \exp[-\beta_n(x-L_x)] \right\} \\
&\times \cos(n\pi y/L_y) \\
&+ d_{mn}^{(r+)} \left\{ \exp[\beta_n(x-L_x)] + b_{mn}^{(-)} \exp[-\beta_n(x-L_x)] \right\} \\
&\times \sin(n\pi y/L_y)
\end{aligned} \tag{3.19}$$

where

$$b_{mn}^{(-)} = \frac{\omega\epsilon_1 Z_c \beta_n \exp(\beta_n d_x) + k_1^2 \exp(\beta_n d_x)}{\omega\epsilon_1 Z_c \beta_n \exp(-\beta_n d_x) - k_1^2 \exp(-\beta_n d_x)}.$$

The amplitude of the evanescent waves is a function of the impedance at the surface of the layer. It is therefore possible to control the amplitude of the edge waves by changing the surface impedance.

Underneath the electrode, the edge waves evanesce in both the x and y directions

$$\begin{aligned}
&\psi_1^{(e)}(x,y) = \\
&\sum_{mn}\left\{c_{mn}^{(x+)}\exp[\beta_n(x-L_x/2)] + c_{mn}^{(x-)}\exp[-\beta_n(x-L_x/2)]\right\} \\
&\times\cos(n\pi y/L_y) \\
&+\left\{c_{mn}^{(y+)}\exp[\beta_m(y-L_y/2)] + c_{mn}^{(y-)}\exp[-\beta_m(y-L_y/2)]\right\} \\
&\times\cos(m\pi x/L_x) \\
&+\left\{s_{mn}^{(x+)}\exp[\beta_n(x-L_x/2)] + s_{mn}^{(x-)}\exp[-\beta_n(x-L_x/2)]\right\} \\
&\times\sin(n\pi y/L_y) \\
&+\left\{s_{mn}^{(y+)}\exp[\beta_m(y-L_y/2)] + s_{mn}^{(y-)}\exp[-\beta_m(y-L_y/2)]\right\} \\
&\times\sin(m\pi x/L_x)
\end{aligned} \tag{3.20}$$

where $\beta_m = \jmath\sqrt{k_2^2-(m\pi/L_x)^2}$ and $\beta_n = \jmath\sqrt{k_2^2-(n\pi/L_y)^2}$. The total electric and magnetic fields are continuous across the electrode edge. This leads to a matrix equation for the unknown coefficients involving the Cosine terms $\mathbf{Z_{mn}C_{mn}} = \mathbf{V_{mn}^{(c)}}$ and the Sine terms $\mathbf{Z_{mn}S_{mn}} = \mathbf{V_{mn}^{(s)}}$. The solutions are $\mathbf{C_{mn}} = \mathbf{Z_{mn}^{-1}V_{mn}^{(c)}}$ and $\mathbf{S_{mn}} = \mathbf{Z_{mn}^{-1}V_{mn}^{(s)}}$. In this way, the edge waves are coupled to the incident standing wave. The same boundary conditions applied to edge waves in the y-direction lead to equivalent systems. The matrices are defined in Appendix B.

3.4.2 Corner Wave

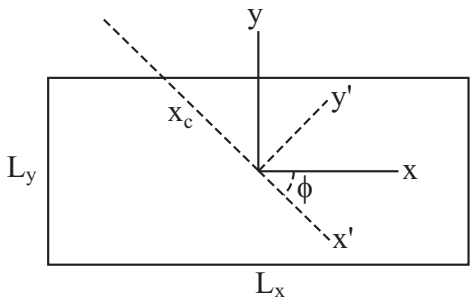

Figure 3.2 Rotated coordinate system for corner wave.

The total potential in region 1 is the superposition of the standing wave, the edge waves,

and a corner wave

$$\psi_1 = \psi_1^{(s)} + \psi_1^{(e)} + \psi_1^{(cr)}. \tag{3.21}$$

The third and final component of the field arises from interactions between edge waves near the corners of the reactor. Here evanescent waves from one edge interfere with the waves tied to the other edge. A rotated coordinate system is necessary to capture the behavior of the corner wave (Figure 3.2). To a good approximation, the corner wave may be decomposed into evanescent waves in the original and rotated coordinate systems

$$\psi_1^{(cr)}(x, y, x', y') = \psi_1^{(c)}(x, y) + \psi_1^{(c\prime)}(x', y'). \tag{3.22}$$

Here

$$\begin{aligned}
&\psi_1^{(c)}(x, y) = \\
&A_c \exp[\jmath k_2(y - L_y/2)] + B_c \exp[-\jmath k_2(y - L_y/2)] \\
&+ C_c \exp[-\jmath k_2(x - L_x/2)] + D_c \exp[\jmath k_2(x - L_x/2)]
\end{aligned}$$

and

$$\begin{aligned}
&\psi_1^{(c\prime)}(x', y') = \\
&A_{c\prime} \exp(\jmath k_2 y') + B_{c\prime} \exp(-\jmath k_2 y') \\
&+ C_{c\prime} \exp(-\jmath k_2 x') + D_{c\prime} \exp(\jmath k_2 x').
\end{aligned}$$

In order to solve for the unknown coefficients, I must consider the behavior of currents induced on the surface of the electrode $\mathbf{J_s}(x, y) = \hat{\mathbf{n}} \times \mathbf{H}(x, y)$ where $\hat{\mathbf{n}} = \hat{\mathbf{z}}$ on the top and $\hat{\mathbf{n}} = -\hat{\mathbf{z}}$ on the bottom. Away from the corners at the electrode edge, current leaving the top sheet reappears on the bottom sheet flowing in the opposite direction. Beginning on the top sheet and moving along an edge, one passes over to the bottom sheet at the corner of the electrode. In order to avoid a discontinuity between currents flowing in opposite directions, the surface current density at the corners of the electrode must vanish. The corner wave is necessary to satisfy this continuity condition.

My strategy for enforcing current continuity at the corner of the electrode is as follows. There are a total of eight components of the magnetic field that must vanish, two for each of the

four corners. The magnetic field at each corner is expressed in the rotated coordinate system. Evanescent waves act to cancel the x'-component at the upper-right and lower-left corners. This leads to the following matrix equation for the $A_{c\prime}$ and $B_{c\prime}$ coefficients $\mathbf{Z}^{(\mathbf{x}\prime)}\mathbf{C}^{(\mathbf{x}\prime)} = \mathbf{V}^{(\mathbf{x}\prime)}$. The impedance matrix is defined thus

$$\mathbf{Z}^{(\mathbf{x}\prime)} = \begin{bmatrix} -k_2 \exp(\jmath k_2 y_c) & k_2 \exp(-\jmath k_2 y_c) \\ k_2 \exp(-\jmath k_2 y_c) & k_2 \exp(\jmath k_2 y_c) \end{bmatrix}$$

where y_c is the distance from the corner to the center in the new coordinate system. Here the vector of unknowns and right hand side are

$$\mathbf{C}^{(\mathbf{x}\prime)} = \begin{bmatrix} A_{c\prime} \\ B_{c\prime} \end{bmatrix}$$

and

$$\mathbf{V}^{(\mathbf{x}\prime)} = -\frac{1}{\omega\epsilon_1} \begin{bmatrix} H^{(e)}_{x\prime}(L_x, L_y) \\ H^{(e)}_{x\prime}(0,0) \end{bmatrix}.$$

A similar system of equations is used to cancel the y'-components at the upper-left and lower-right corners $\mathbf{Z}^{(\mathbf{y}\prime)}\mathbf{C}^{(\mathbf{y}\prime)} = \mathbf{V}^{(\mathbf{y}\prime)}$ where

$$\mathbf{Z}^{(\mathbf{y}\prime)} = \begin{bmatrix} -k_2 \exp(\jmath k_2 y_c) & k_2 \exp(-\jmath k_2 y_c) \\ -k_2 \exp(-\jmath k_2 y_c) & k_2 \exp(\jmath k_2 y_c) \end{bmatrix},$$

$$\mathbf{C}^{(\mathbf{y}\prime)} = \begin{bmatrix} C_{c\prime} \\ D_{c\prime} \end{bmatrix},$$

and

$$\mathbf{V}^{(\mathbf{y}\prime)} = -\frac{1}{\omega\epsilon_1} \begin{bmatrix} H^{(e)}_{y\prime}(0, L_y) \\ H^{(e)}_{y\prime}(L_x, 0) \end{bmatrix}.$$

The remaining four magnetic field components are similarly canceled by evanescent waves in the original coordinate system

$$\begin{aligned} \psi_1^{(c)}(x,y) =& A_c \exp[\jmath k_2 (y - L_y/2)] \\ &+ B_c \exp[-\jmath k_2 (y - L_y/2)] \\ &+ C_c \exp[-\jmath k_2 (x - L_x/2)] \\ &+ D_c \exp[\jmath k_2 (x - L_x/2)]. \end{aligned} \tag{3.23}$$

The unprimed unknowns satisfy the following matrix equation $\mathbf{Z^{(y)}C^{(y)}} = \mathbf{V^{(y)}}$ where

$$\mathbf{Z^{(y)}} = \begin{bmatrix} k_2 \exp(\jmath k_2 L_y/2) & -k_2 \exp(-\jmath k_2 L_y/2) \\ k_2 \exp(-\jmath k_2 L_y/2) & -k_2 \exp(\jmath k_2 L_y/2) \end{bmatrix},$$

$$\mathbf{C^{(y)}} = \begin{bmatrix} A_c \\ B_c \end{bmatrix},$$

and

$$\mathbf{V^{(y)}} = \frac{1}{\omega\epsilon_1} \begin{bmatrix} H_{y\prime}(L_x, L_y)\sin(\pi/2 - \phi) \\ H_{y\prime}(0,0)\sin(\pi/2 - \phi) \end{bmatrix}.$$

Also $\mathbf{Z^{(x)}C^{(x)}} = \mathbf{V^{(x)}}$ where

$$\mathbf{Z^{(x)}} = \begin{bmatrix} k_2 \exp(\jmath k_2 L_x/2) & -k_2 \exp(-\jmath k_2 L_x/2) \\ k_2 \exp(-\jmath k_2 L_x/2) & -k_2 \exp(\jmath k_2 L_x/2) \end{bmatrix},$$

$$\mathbf{C^{(x)}} = \begin{bmatrix} C_c \\ D_c \end{bmatrix},$$

and

$$\mathbf{V^{(x)}} = \frac{-1}{\omega\epsilon_1} \begin{bmatrix} H_{x\prime}(L_x, L_y)\cos(\pi/2 - \phi) \\ H_{x\prime}(0,0)\cos(\pi/2 - \phi) \end{bmatrix}.$$

After solving for the unknown coefficients I are able to calculate the total potential over the surface of the antenna. It remains to determine the angle (ϕ) defining the primed coordinates (Figure 3.2). To this end, I solve for the corner-wave coefficients for a range of angles. Then I choose the angle that minimizes the magnitude of the surface current density $\mathbf{J_s}(x, y)$ at the corners of the electrode.

3.5 Results

3.5.1 Film Deposition

It is instructive to compare an experimental film deposition with my theoretical power distribution as the thickness of the film at a given point is proportional to the power delivered to that point.[18] . A rectangular PECVD system was used to deposit a layer of a-Si on an

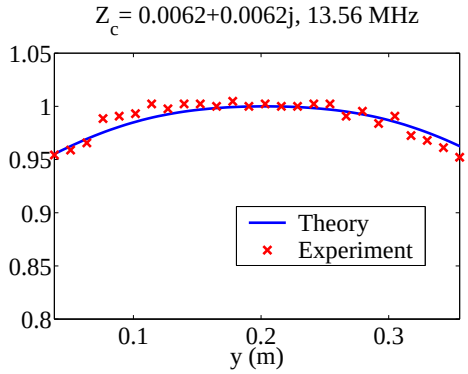

Figure 3.3 Normalized theoretical power and experimental deposition thickness in the y-direction at x=$L_x/2$. The aluminum electrode of dimensions 55.8×40.6 cm^2 was center-fed by a point source on the back side. An 11:1 hydrogen to silane ratio was maintained at a base pressure of 530 mTorr for 10 minutes during the deposition.

aluminum substrate at 13.56 MHz. The aluminum electrode of dimensions 55.8×40.6 cm^2 was center-fed by a point source on the back side. The permittivity of the stainless steel sidewalls was calculated using $\epsilon_{cr} = 1 - \jmath\sigma_c/\epsilon_0\omega$ where the conductivity was $\sigma_c = 1.4$E6 siemens/m. The gap between the edge of the electrode and the sidewalls was 6.3 cm in the x-direction and 2.5 cm in the y-direction. An 11:1 hydrogen to silane ratio was maintained at a base pressure of 530 mTorr for 10 minutes during the deposition. A showerhead was used to evenly distribute the reactive gases above the electrode.

Since the theoretical power distribution is sensitive to the electron density n_e this parameter must be chosen with care. I estimate the electron density of my plasma to be n_e =3.5E8 cm^{-3} based on a chamber pressure of 530 mTorr and my experimental data. Figure 3.3 shows the normalized theoretical power and measured a-Si thickness in the y-direction. The theoretical and experimental data are in good agreement. Minor discrepancies may be attributed to noise in the measurements. Figure 3.4 shows the theoretical power over the surface of the electrode at 13.56 and 40.68 MHz. The nonuniformity of the field may be quantified thus

$$U = \left| \frac{\max[P(x,y)] - \min[P(x,y)]}{\max[P(x,y)] + \min[P(x,y)]} \right| \times 100\%. \tag{3.24}$$

Here $P(x,y)$ is the power as a function of position. The position (x,y) ranges over the whole

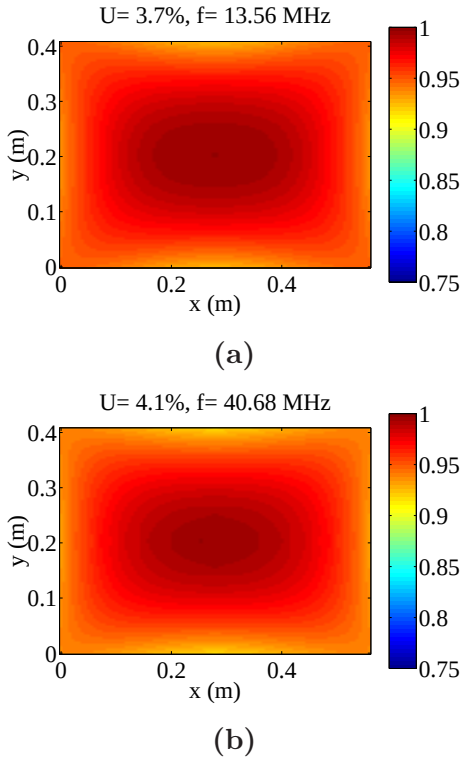

Figure 3.4 Normalized theoretical power at 13.56(a) and 40.68(b) MHz.

surface of the electrode. The nonuniformity is slightly greater at 40.68 MHz than at 13.56 MHz. At 40.68 MHz, the wavelength is shorter and the standing wave is concentrated toward the center of the reactor.

3.5.2 Control of Nonuniformity

Uniformity is even more problematic for electrodes with large aspect ratios. Consider the power distribution for the rectangular electrode in Figure 3.5. The antenna is again fed by a line source in the center. The gap between the edge of the electrode and the sidewall is 1.3 cm in the x-direction and 3.8 cm in the y-direction. The total field is composed of a standing wave and evanescent waves. Traveling waves originate from the feed, propagate along the surface of the antenna, and constructively interfere at the center of the reactor. The superposition of waves propagating in opposite directions forms a standing wave.

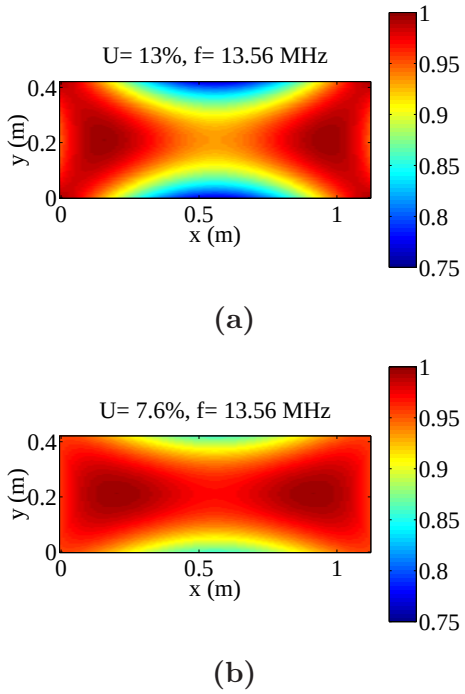

Figure 3.5 Normalized theoretical power for 111.7 × 41.9 cm^2 electrode with bare(a) and coated(b) sidewalls.

For electrically large reactors, the standing wave varies significantly over the surface of the electrode. Nonuniformity is a strong function of frequency for such systems. However, edge effects dominate the field distribution so long as the reactor dimensions remain small with respect to wavelength. The standing wave is essentially constant for electrode sizes less than $\lambda/10$.

For the case of the rectangular reactor with stainless steel sidewalls, the nonuniformity is around 13% (Figure 3.5a). Uniformity can be improved by creating an impedance boundary condition at the plasma edge by adding a lossy layer to the reactor sidewalls. Figure 3.5b shows the power distribution with a 2 mm thick layer attached to the reactor sidewalls. I choose a magnetic material with relative permeability $\mu_{cr} = 205 - \jmath 80$. Comparable material parameters have been realized at 13.56 MHz using ferrites.[27] Clearly, nonuniformity decreases with increasing layer thickness (Figure 3.6a). This trend may be explained as follows. Since the

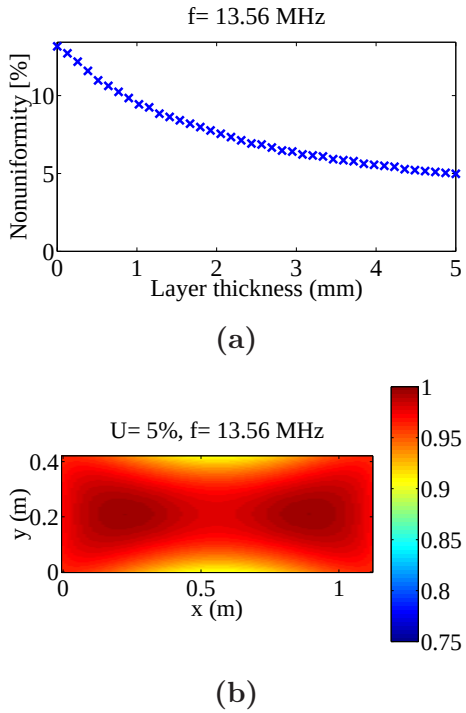

Figure 3.6 Theoretical nonuniformity as a function of layer thickness(a) and normalized theoretical power for a 5 mm thick layer(b).

z-component of the electric field of the edge waves is opposed to the incident field, the edge waves act to reduce the field near the sidewalls. The magnetic material absorbs energy that would otherwise be reflected back under the electrode. Very thin layers reflect more energy as the total electric field remains small at the plasma edge. Figure 3.6b shows the normalized electric field for a 5 mm thick layer. Note how the power along the long edges has increased. The lossy layer creates an IBC on the sidewall that reduces the amplitude of the edge waves and increases the total field near the edges. Nonuniformity is well below the industrial limit of 10% for layers thicker than 1 mm.

3.6 Conclusions

The electromagnetic fields in rectangular plasma reactors have been studied under the homogeneous plasma slab approximation. The Fourier series coefficients of the standing wave

have been determined in the sheath and in the plasma. I have shown that the each Fourier component excites an edge wave in order to satisfy boundary conditions at the plasma edge. The standing wave and edge waves interact to produce a corner wave that ensures current continuity between the top and bottom surfaces of the electrode. Placing a lossy layer on the reactor sidewalls creates an impedance boundary condition at the plasma edge. The amplitude of the edge waves may be controlled by changing the impedance of the layer. The IBC leads to nonuniformities well within industrial tolerances.

CHAPTER 4 Modal analysis of extraordinary optical transmission through a silver film perforated by an infinite square array of circular holes

4.1 Literature Review

Structured noble metals have been the subject of much interest in recent years due to their potential as nanophotonic devices.[28] A number of useful optical properties of such metals have been observed. Nanometallic objects are able to trap incident radiation, focusing it into very small volumes. Krenn *et al.*[29] report enhancement of over 600% in a chain of nanometer scale gold particles. The ability to confine light to very small scales circumvents a fundamental limitation of dielectric waveguides. In order for a mode to propagate along a waveguide with a dielectric core, the diameter of the core must be greater than half a wavelength in the core medium $d_{core} \geq \lambda_0/(2n_{core})$, the so-called diffraction limit. Here d_{core} is the core diameter, λ_0 is the free space wavelength, and n_{core} is the refractive index of the core. Due to the fact that their permittivity is negative at optical frequencies, conservation of momentum dictates that noble metals be able to support guided modes for smaller core diameters. Several plasmonic waveguide geometries have been proposed, including nanowires[30] and stripes.[31] Maier *et al.* demonstrate local energy transport along a waveguide consisting of silver rods.[32] As the losses in the metal limit propagation length, metal-insulator-metal (MIM) waveguides have also been studied.[33] Such waveguides typically consist of a dielectric layer sandwiched between two metal stripes. In MIM waveguides, coupling between surface plasma polaritons on opposite metal surfaces confines the mode to the dielectric region where resistive losses are smaller.

Recently, interesting optical properties of a thin silver film perforated by a periodic array of circular holes have been noted (Figure 4.1). This geometry has been intensely studied since the discovery that such arrays of subwavelength holes allow much greater optical transmission[34]

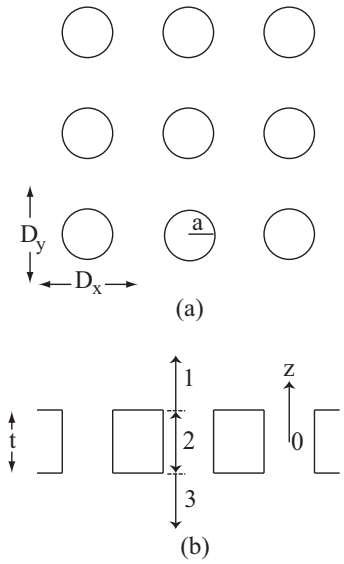

Figure 4.1 Top(a) and side(b)-view of silver film perforated by an infinite array of circular holes. The region above the film is designated 1, inside the hole 2, and below the film 3.

than single holes.[35] Much experimental and theoretical effort has been focused on understanding this extraordinary optical transmission (EOT). Numerical studies of periodic hole arrays have been made using the finite-difference time-domain (FDTD) method. Baida *et al.* study zero-order transmission efficiency through a gold film as a function of incident wavelength.[36] They demonstrate that transmission efficiency can be improved by replacing the holes with an array of annular apertures. Similar structures have been studied in the frequency-domain via scattering matrix methods.[37] Biswas *et al.* leverage the scattering matrix approach to study a subwavelength triangular lattice of holes in a platinum film coupled to a silicon photonic crystal.[38] Their model predicts a resonant absorption of incident radiation over infrared frequencies.

Martin-Moreno *et al.* have studied scattering by a subwavelength square lattice of circular holes in a silver film via mode-matching.[39] Their approach may be summarized as follows. Above and below the film, the fields are expanded in terms of TM and TE Floquet harmonics. Waveguide modes are used inside the hole where the walls are treated as a perfect electric conductor (PEC). The unknown coefficients are found by enforcing boundary conditions at

the upper and lower surfaces of the film. While the silver is treated as a PEC in [39], it is replaced with an impedance boundary condition (IBC) on the top and bottom surfaces of the film in [40]. The walls of the hole remain perfectly conducting, however. Zhang et al.[41] conduct a similar theoretical study of EOT through an array of circular holes. In their approach, the waveguide modes are determined by assuming an exponentially decaying field outside the hole rather than imposing an impedance boundary condition on the wall. While this approach is exact for an isolated hole, the assumption that the field in the metal can be modeled by a Hankel function with an imaginary argument may be problematic for a periodic geometry. Their approach agrees well with experimental data with respect to the position of transmission peaks and nulls. However, no quantitative measure of the error in the peak amplitudes is given. Impedance boundary conditions were also used to analyze transmission through an array of rectangular holes.[42] The assumption of an impedance boundary condition on the hole wall yields excellent quantitative results. Both the position and amplitude of the transmission peaks agree well with experiment.

This chapter extends the formalism in [40] to include an IBC on the walls of the hole. The addition of an impedance boundary condition on the hole walls is a significant improvement as it allows for a finite tangential electric field on the wall surface. It also avoids the necessity to phenomenologically enlarge the holes to capture penetration into the metal.[46] The results herein predict a peak transmission that is much closer to the experimental value than that presented in the cited modal approaches. While previous mode-matching studies predict similar qualitative results, the theory presented here permits accurate quantitative study of the EOT phenomenon. In addition, this approach avoids any explicit assumptions regarding the form of the solution in the metal region. The chapter is organized as follows. Section 4.2 introduces the scalar decomposition used to split the fields into TE and TM components. Section 4.3 details the derivation of the waveguide modes in the hole region with an impedance boundary condition on the walls. The modal expansions above and below the film and in the hole region are discussed in Section 4.4. A set of matrix equations for the unknown coefficients is solved in Section 4.5. Section 4.6 includes a discussion of the results, while the conclusions are collected

in Section 4.7.

4.2 Scalar Decomposition

For a preferred direction along the z-axis, the frequency-domain electric and magnetic fields may be written in terms of transverse magnetic (TM) and transverse electric (TE) scalar potentials thus[1]

$$\mathbf{E} = \nabla \times \nabla \times [\hat{\mathbf{z}}\psi] + \imath\omega\mu_p \nabla \times [\hat{\mathbf{z}}\varphi] \tag{4.1}$$

$$\mathbf{H} = -\imath\omega\epsilon_p \nabla \times [\hat{\mathbf{z}}\psi] + \nabla \times \nabla \times [\hat{\mathbf{z}}\varphi]. \tag{4.2}$$

Here ω is the frequency and ϵ_p, μ_p are respectively the permittivity and permeability of region p. Cylindrical coordinates are employed inside the hole. In cylindrical coordinates, the components of the electric and magnetic fields are

$$E_z = \left(\frac{\partial^2}{\partial z^2} + k_p^2\right)\psi \tag{4.3}$$

$$E_\rho = \frac{\partial^2 \psi}{\partial \rho \partial z} + \imath\omega\mu_p \frac{1}{\rho}\frac{\partial \varphi}{\partial \phi} \tag{4.4}$$

$$E_\phi = \frac{1}{\rho}\frac{\partial^2 \psi}{\partial \phi \partial z} - \imath\omega\mu_p \frac{\partial \varphi}{\partial \rho} \tag{4.5}$$

$$H_z = \left(\frac{\partial^2}{\partial z^2} + k_p^2\right)\varphi \tag{4.6}$$

$$H_\rho = -\imath\omega\epsilon_p \frac{1}{\rho}\frac{\partial \psi}{\partial \phi} + \frac{\partial^2 \varphi}{\partial \rho \partial z} \tag{4.7}$$

$$H_\phi = \imath\omega\epsilon_p \frac{\partial \psi}{\partial \rho} + \frac{1}{\rho}\frac{\partial^2 \varphi}{\partial \phi \partial z} \tag{4.8}$$

where $k_p^2 = \omega^2 \epsilon_p \mu_p$. Above and below the film, the scalar potentials and fields are expressed in Cartesian coordinates

$$E_x = \frac{\partial^2 \psi}{\partial x \partial z} + \imath\omega\mu_p \frac{\partial \varphi}{\partial y} \tag{4.9}$$

$$E_y = \frac{\partial^2 \psi}{\partial y \partial z} - \imath\omega\mu_p \frac{\partial \varphi}{\partial x} \tag{4.10}$$

$$E_z = \left(\frac{\partial^2}{\partial^2 z} + k_p^2\right)\psi \tag{4.11}$$

$$H_x = \frac{\partial^2 \varphi}{\partial x \partial z} - \imath\omega\epsilon_p \frac{\partial \psi}{\partial y} \tag{4.12}$$

$$H_y = \frac{\partial^2 \varphi}{\partial y \partial z} + \imath\omega\epsilon_p \frac{\partial \psi}{\partial x} \tag{4.13}$$

$$H_z = \left(\frac{\partial^2}{\partial^2 z} + k_p^2\right)\varphi. \tag{4.14}$$

The strategy for finding the potentials is as follows. Above and below the film, the Bloch-Floquet theorem guarantees a complete discrete basis set consisting of TE and TM Floquet modes.[43] Inside the hole, I expand the fields in terms of waveguide modes derived by imposing an impedance boundary condition on the hole wall. For azimuthal numbers other than zero, these waveguide modes involve coupled TE and TM potentials. As the hole region is radially finite, the waveguide modes are also a complete discrete basis.[3] The unknown coefficients are determined by enforcing boundary conditions on the upper and lower horizontal interfaces over a single unit cell.

4.3 Waveguide modes

First I must determine the eigenmodes of the hole region while imposing an impedance boundary condition on the walls. I begin by writing the TM and TE potentials as Fourier series

$$\psi_h(\rho, \phi, z) = \sum_{n=-\infty}^{\infty} a_n \mathrm{J}_n(\gamma\rho) \exp(\imath n\phi) \exp(\imath\beta z) \tag{4.15}$$

$$\varphi_h(\rho, \phi, z) = \sum_{n=-\infty}^{\infty} b_n \mathrm{J}_n(\gamma\rho) \exp(\imath n\phi) \exp(\imath\beta z) \tag{4.16}$$

where $\mathrm{J}_n(\gamma\rho)$ is the Bessel function of the first kind, n is an integer, β is the axial wavenumber, $\gamma^2 = k^2 - \beta^2$, and a_n and b_n are unknown coefficients. On the walls of the hole we impose the

following impedance boundary condition

$$\mathbf{E}_{tan} = Z\hat{\mathbf{n}} \times \mathbf{H} \tag{4.17}$$

where $\hat{\mathbf{n}}$ is a unit vector normal to the surface and $Z = \sqrt{\mu_m/\epsilon_m}$ is the surface impedance of the metal. In this case $\hat{\mathbf{n}} = -\hat{\boldsymbol{\rho}}$. We employ the Drude free electron model[26] for the silver permittivity

$$\epsilon_{mr} = 1 - \frac{\omega_p^2}{(\omega^2 + \imath\gamma_p\omega)} \tag{4.18}$$

where γ_p is a damping coefficient and the plasma frequency $\omega_p = 2\pi(8980)\sqrt{n_e}$ depends on the electron number density n_e. Here the damping coefficient $\gamma_p = 9 \times 10^{13}$ and the plasma frequency $\omega_p = 1.37 \times 10^{16}$. The IBC (4.17) leads to two equations

$$E_z(a) = -ZH_\phi(a) \tag{4.19}$$

and

$$E_\phi(a) = ZH_z(a). \tag{4.20}$$

Substituting (4.15) and (4.16) into (4.19) and (4.20) and exploiting orthogonality yields

$$\left[\gamma^2 \mathrm{J}_n(\gamma a) + \imath Z\omega\epsilon\gamma \mathrm{J}_n'(\gamma a)\right] a_n - Z\beta n/a \mathrm{J}_n(\gamma a) b_n = 0 \tag{4.21}$$

and

$$\beta n/a \mathrm{J}_n(\gamma a) a_n + \left[\imath\omega\mu\gamma \mathrm{J}_n'(\gamma a) + Z\gamma^2 \mathrm{J}_n(\gamma a)\right] b_n = 0. \tag{4.22}$$

The system may be rewritten in matrix form $\mathbf{Z_n C_n} = \mathbf{0}$. Here

$$\mathbf{C_n} = \begin{bmatrix} a_n \\ \\ b_n \end{bmatrix}. \tag{4.23}$$

We find the eigenvalues by sweeping over the axial wavenumber β to find the zeros of the determinant of the system matrix $\mathbf{Z_n}$

$$\left[\gamma^2 \mathrm{J}_n(\gamma a) + \imath Z\omega\epsilon\gamma \mathrm{J}_n'(\gamma a)\right] \left[\imath\omega\mu\gamma \mathrm{J}_n'(\gamma a) + Z\gamma^2 \mathrm{J}_n(\gamma a)\right] + Z\beta^2 n^2/a^2 \mathrm{J}_n^2(\gamma a) = 0. \tag{4.24}$$

The coefficients a_{nj} and b_{nj} are found from the eigenvectors of $\mathbf{Z_n}$, where the second subscript indexes the eigenvalue β_{nj} associated with eigenvector $\mathbf{C_{nj}}$.

Each mode was subsequently normalized by ensuring the following orthogonality condition was satisfied

$$\int_0^{2\pi}\int_0^a \hat{\mathbf{z}}\cdot\mathbf{E}_p\times\mathbf{H}_q^*\rho d\rho d\phi = \begin{cases}\delta_{pq}, & \Im\{\beta_{p,q}\}=0\\ -\imath\delta_{pq}, & \Im\{\beta_{p,q}\}>0\end{cases} \tag{4.25}$$

where $\mathbf{E}_p$ is the electric field due to the waveguide mode mi, $\mathbf{H}_q$ is the magnetic field due waveguide mode nj, and $\beta_{p,q}$ are the eigenvalues for mode p and q, respectively. The first case where $\Im\{\beta_{p,q}\}=0$ corresponds to propagating modes. Such modes carry real power in the direction of propagation. The condition $\Im\{\beta_{p,q}\}>0$ identifies modes that evanesce in the z-direction. Evanescent modes carry imaginary power along axis of the waveguide which accounts for the factor of $\imath$ multiplying the delta function in equation (4.25). Once (4.25) is satisfied, the resulting modes form a complete orthonormal basis over the area of the hole.

The evolution of the modes from decoupled TE and TM modes in the case of perfectly conducting walls to hybrid modes in the IBC case is of some interest. Note that when the surface impedance Z is set to zero, equation (4.24) reduces to

$$\mathrm{J}_n(\gamma a)\mathrm{J}_n'(\gamma a)=0. \tag{4.26}$$

Two families of solutions result. The eigenvalues of the TM modes for a PEC guide are obtained from the zeros of the Bessel function, while the eigenvalues of the TE modes may be obtained from the zeros of the first derivative of the Bessel function. Thus equation (4.24) may be viewed as a generalization of the characteristic equation for the eigenvalues of a circular PEC waveguide.

The polarization of the incident field, together with symmetry considerations, determines the modes that are excited inside the hole. The azimuthal symmetry of the hole dictates that the overlap integrals between the incident field and the hybrid modes vanish for azimuthal numbers other than $n=1$ or $n=-1$. Therefore, there is a strong coupling between the doubly-degenerate $n=1$ mode and the incident plane wave.

4.4 Eigenfunction expansions

4.4.1 Incident field

The excitation is a plane wave of arbitrary angle and frequency incident from region 1. Define the following rotation matrices:

$$\mathbf{R}^{(\phi_0)} = \begin{bmatrix} \cos(\phi_0) & \sin(\phi_0) & 0 \\ -\sin(\phi_0) & \cos(\phi_0) & 0 \\ 0 & 0 & 1 \end{bmatrix} \tag{4.27}$$

and

$$\mathbf{R}^{(\theta_0)} = \begin{bmatrix} 1 & 0 & 0 \\ 0 & \cos(\theta_0) & \sin(\theta_0) \\ 0 & -\sin(\theta_0) & \cos(\theta_0) \end{bmatrix} \tag{4.28}$$

along with the vectors

$$\mathbf{k}^{(0)} = \begin{bmatrix} k_x^0 \\ k_y^0 \\ k_z^0 \end{bmatrix} \tag{4.29}$$

and

$$\mathbf{P}^{(0)} = \begin{bmatrix} \cos(\alpha_0) \\ \sin(\alpha_0) \\ 0 \end{bmatrix}. \tag{4.30}$$

Here the incident propagation direction vector $\mathbf{k}^{(0)}$ is defined by

$$\mathbf{k}^{(0)} = -\begin{bmatrix} \sin(\theta_0)\cos(\phi_0) \\ \sin(\theta_0)\sin(\phi_0) \\ \cos(\theta_0) \end{bmatrix}. \tag{4.31}$$

The incident electric and magnetic fields are given by $\mathbf{E}^{(0)} = \mathbf{R}^{(\theta_0)}\mathbf{R}^{(\phi_0)}\mathbf{P}^{(0)}$ and $\mathbf{H}^{(0)} = k\mathbf{k}^{(0)} \times \mathbf{E}^{(0)}/(\omega\mu_0)$.

4.4.2 Regions 1 and 3

Above and below the film, the fields are expanded in terms of TM and TE Floquet modes:

$$\psi_{mn}^{(1,3)}(x,y,z) = A_{mn}^{(1,3)} \exp[\imath \mathbf{k_{mn}} \cdot \boldsymbol{\rho} \pm \imath \beta_{mn}(z \mp t/2)]/\sqrt{D_x D_y} \tag{4.32}$$

and

$$\varphi_{mn}^{(1,3)}(x,y,z) = B_{mn}^{(1,3)} \exp[\imath \mathbf{k_{mn}} \cdot \boldsymbol{\rho} \pm \imath \beta_{mn}(z \mp t/2)]/\sqrt{D_x D_y} \tag{4.33}$$

where $\mathbf{k_{mn}} = 2\pi(m\hat{\mathbf{x}}/D_x + n\hat{\mathbf{y}}/D_y)$, $\boldsymbol{\rho} = x\hat{\mathbf{x}} + y\hat{\mathbf{y}}$, $\beta_{mn}^2 = k^2 - (2\pi m/D_x)^2 - (2\pi n/D_y)^2$, and $A_{mn}^{(1,3)}$ and $B_{mn}^{(1,3)}$ are unknown coefficients. The transverse electric and magnetic fields associated with each mode are given by

$$\mathbf{E}_{tmn}^{(1,3)\prime}(x,y,z) = \mp(\beta_{mn}k_x\hat{\mathbf{x}} + \beta_{mn}k_y\hat{\mathbf{y}})\psi_{mn}^{(1,3)}(x,y,z), \tag{4.34}$$

$$\mathbf{H}_{tmn}^{(1,3)\prime}(x,y,z) = (\omega\epsilon k_y\hat{\mathbf{x}} - \omega\epsilon k_x\hat{\mathbf{y}})\psi_{mn}^{(1,3)}(x,y,z), \tag{4.35}$$

$$\mathbf{E}_{tmn}^{(1,3)\prime\prime}(x,y,z) = (-\omega\mu k_y\hat{\mathbf{x}} + \omega\mu k_x\hat{\mathbf{y}})\varphi_{mn}^{(1,3)}(x,y,z), \tag{4.36}$$

and

$$\mathbf{H}_{tmn}^{(1,3)\prime\prime}(x,y,z) = \mp(\beta_{mn}k_x\hat{\mathbf{x}} + \beta_{mn}k_y\hat{\mathbf{y}})\varphi_{mn}^{(1,3)}(x,y,z) \tag{4.37}$$

where $k_x = 2\pi m/D_x$ and $k_y = 2\pi n/D_y$. When $m = n = 0$, two additional modes are necessary to span the space

$$\begin{aligned} \mathbf{E}^{(1,3)\prime}(z) &= A_{00}^{(1,3)} \exp[\pm\imath k(z \mp t/2)]\hat{\mathbf{x}} \\ \mathbf{H}^{(1,3)\prime}(z) &= \pm k/(\omega\mu) A_{00}^{(1,3)} \exp[\pm\imath k(z \mp t/2)]\hat{\mathbf{y}} \end{aligned} \tag{4.38}$$

and

$$\begin{aligned} \mathbf{E}^{(1,3)\prime\prime}(z) &= B_{00}^{(1,3)} \exp[\pm\imath k(z \mp t/2)]\hat{\mathbf{y}} \\ \mathbf{H}^{(1,3)\prime\prime}(z) &= \mp k/(\omega\mu) B_{00}^{(1,3)} \exp[\pm\imath k(z \mp t/2)]\hat{\mathbf{x}}. \end{aligned} \tag{4.39}$$

As many thin films are deposited on glass substrates, it is worth describing how the formulation could be modified to include a dielectric layer beneath the silver. The additional layer introduces four unknown coefficients for each Floquet harmonic indexed mn

$$\psi_{mn}^{(s)}(x,y,z) = A_{mn}^{(s\pm)} \exp[\imath \mathbf{k_{mn}} \cdot \boldsymbol{\rho} \pm \imath \beta_{mn}^{(s)}(z - t_s)]/\sqrt{D_x D_y} \tag{4.40}$$

and

$$\varphi_{mn}^{(s)}(x,y,z) = B_{mn}^{(s\pm)} \exp[\imath \mathbf{k_{mn}} \cdot \boldsymbol{\rho} \pm \imath \beta_{mn}^{(s)}(z - t_s)]/\sqrt{D_x D_y} \tag{4.41}$$

where t_s is the height of the layer. These unknowns are associated with two modes (TE and TM) propagating in the positive z-direction, as well as two modes (TE and TM) propagating in the negative z-direction. These Floquet harmonics are identical to those in the air region with the exception that the z-component of the wave vector must be modified such that the Helmholtz equation is satisfied in the substrate, $\beta_{mn}^{(s)} = [k_s^2 - (2\pi m/D_x)^2 - (2\pi n/D_y)]^{1/2}$. Here $\beta_{mn}^{(s)}$ is the z-component of the wave vector and k_s is the wavenumber in the substrate. One observes a red-shift in the position of the first-order SPP transmission peak that is proportional to the refractive index of the substrate.[44] The effect of a substrate on the transmission profile may be utilized by practical devices. The change in position of the resonant peak can be used to tune the response of the structure for sensing purposes.

4.4.3 Region 2

Inside the hole, I expand the fields in a series consisting of the waveguide modes defined in Section 4.3. The transverse components of the total field inside the hole are therefore

$$\mathbf{E}_t^{(2)}(\rho,\phi,z) = \sum_{nj} [C_{nj} \exp(\imath \beta_{nj} z) + D_{nj} \exp(-\imath \beta_{nj} z)][E_{\rho nj}(\rho)\hat{\boldsymbol{\rho}} + E_{\phi nj}(\rho)\hat{\boldsymbol{\phi}}] \exp(\imath n\phi) \tag{4.42}$$

and

$$\mathbf{H}_t^{(2)}(\rho,\phi,z) = \sum_{nj} [C_{nj} \exp(\imath \beta_{nj} z) - D_{nj} \exp(-\imath \beta_{nj} z)][H_{\rho nj}(\rho)\hat{\boldsymbol{\rho}} + H_{\phi nj}(\rho)\hat{\boldsymbol{\phi}}] \exp(\imath n\phi) \tag{4.43}$$

where

$$E_{\rho nj}(\rho) = \imath \beta_{nj} \gamma_{nj} \mathrm{J}_n'(\gamma_{nj}\rho) a_{nj} - \omega \mu n \mathrm{J}_n(\gamma_{nj}\rho)/\rho b_{nj} \tag{4.44}$$

$$E_{\phi nj}(\rho) = -n\beta_{nj} \mathrm{J}_n(\gamma_{nj}\rho)/\rho a_{nj} - \imath \omega \mu \gamma_{nj} \mathrm{J}_n'(\gamma_{nj}\rho) b_{nj} \tag{4.45}$$

$$H_{\rho nj}(\rho) = \omega \epsilon n \mathrm{J}_n(\gamma_{nj}\rho)/\rho a_{nj} + \imath \beta_{nj} \gamma_{nj} \mathrm{J}_n'(\gamma_{nj}\rho) b_{nj} \tag{4.46}$$

$$H_{\phi nj}(\rho) = \imath \omega \epsilon \gamma_{nj} \mathrm{J}_n'(\gamma_{nj}\rho) a_{nj} - \beta_{nj} n \mathrm{J}_n(\gamma_{nj}\rho)/\rho b_{nj} \tag{4.47}$$

and C_{nj} and D_{nj} are unknown waveguide mode coefficients.

4.5 Matrix Equations

I enforce an impedance boundary condition on the metal-air interfaces and continuity of the tangential electric field over the hole area at $z = \pm t/2$:

$$\mathbf{E}_t^{(1,3)} = \begin{cases} \pm Z\hat{\mathbf{z}} \times \mathbf{H}^{(1,3)}, & \rho \geq a \\ \mathbf{E}_t^{(2)}(\pm t/2), & \rho < a. \end{cases} \tag{4.48}$$

Testing (4.48) with the appropriate TM or TE mode leads to the following matrix equations

$$\mathbf{Z}^{(e1)}\mathbf{A} + \mathbf{V}^{(e0)} = \mathbf{M}^{(e1)}\left[\mathbf{D}^{(1)}\mathbf{C}^{(+)} + \mathbf{D}^{(2)}\mathbf{C}^{(-)}\right] \tag{4.49}$$

and

$$\mathbf{Z}^{(e2)}\mathbf{B} = \mathbf{M}^{(e2)}\left[\mathbf{D}^{(2)}\mathbf{C}^{(+)} + \mathbf{D}^{(1)}\mathbf{C}^{(-)}\right]. \tag{4.50}$$

The matrices

$$Z_{uv}^{(e1)} = \int_U \mathbf{H}_u \cdot \mathbf{E}_v^{(1)} dxdy - Z\int_S \mathbf{H}_u \cdot \hat{\mathbf{z}} \times \mathbf{H}_v^{(1)} dxdy \tag{4.51}$$

and

$$M_{uv}^{(e1)} = \int_H \mathbf{H}_u \cdot \mathbf{E}_v^{(2)} \rho d\rho d\phi \tag{4.52}$$

contain the overlap integrals between testing $\mathbf{H}_u = \hat{\mathbf{z}} \times \mathbf{H}_{tmn}^*$ and basis functions $\mathbf{E}_v^{(1,3)} = \mathbf{E}_{tpq}^{(1,3)}$ and $\mathbf{H}_v^{(1,3)} = \mathbf{H}_{tpq}^{(1,3)}$. Here $\mathbf{E}_v^{(2)} = E_{\rho nj}(\rho)\hat{\boldsymbol{\rho}} + E_{\phi nj}(\rho)\hat{\boldsymbol{\phi}}$ is the electric field associated with a waveguide mode, U is the area of the unit cell, S is the area covered by the metal, and H is the area of the hole. The integrals over the azimuthal direction were calculated analytically while the remaining integral over the radial direction was computed by quadrature. The matrices $D_{vv}^{(1,2)} = \exp(\pm \imath \beta_{nj} t/2)$ contain phase terms for each waveguide mode. The overlap integrals between region 2 and 3 are included in

$$Z_{uv}^{(e2)} = \int_U \mathbf{H}_u \cdot \mathbf{E}_v^{(3)} dxdy - Z\int_S \mathbf{H}_u \cdot \hat{\mathbf{z}} \times \mathbf{H}_v^{(3)} dxdy \tag{4.53}$$

and

$$M_{uv}^{(e2)} = \int_H \mathbf{H}_u \cdot \mathbf{E}_v^{(2)} \rho d\rho d\phi. \tag{4.54}$$

The overlap between testing functions and the incident field is contained in the vector

$$V_u^{(e0)} = \int_U \mathbf{H}_u \cdot \mathbf{E}^{(0)} dxdy - Z\int_S \mathbf{H}_u \cdot \hat{\mathbf{z}} \times \mathbf{H}^{(0)} dxdy. \tag{4.55}$$

The vector $\mathbf{A}$ contains the unknowns from region 1, $\mathbf{B}$ contains the unknowns from region 3, and $C_v^{(+)} = C_{nj}$ and $C_v^{(-)} = D_{nj}$ are the unknown waveguide mode amplitudes.

Continuity of the tangential components of the magnetic field is enforced over the hole area only

$$\mathbf{H}_t^{(1,3)} = \mathbf{H}_t^{(2)}(\pm t/2), \quad \rho < a. \tag{4.56}$$

Testing the magnetic field with waveguide modes leads to the following matrix equations:

$$\mathbf{M}^{(h1)}\mathbf{A} + \mathbf{V}^{(h0)} = \mathbf{D}^{(1)}\mathbf{C}^{(+)} - \mathbf{D}^{(2)}\mathbf{C}^{(-)} \tag{4.57}$$

$$\mathbf{M}^{(h2)}\mathbf{B} = \mathbf{D}^{(2)}\mathbf{C}^{(+)} - \mathbf{D}^{(1)}\mathbf{C}^{(-)} \tag{4.58}$$

where

$$M_{uv}^{(h1)} = \int_H \mathbf{E}_u \cdot \mathbf{H}_v^{(1)} \rho d\rho d\phi \tag{4.59}$$

and

$$M_{uv}^{(h2)} = \int_H \mathbf{E}_u \cdot \mathbf{H}_v^{(3)} \rho d\rho d\phi \tag{4.60}$$

contain the overlap integrals between regions 1 and 2 and 2 and 3, respectively. Here we test with the electric field of a waveguide mode given by $\mathbf{E}_u = -\hat{\mathbf{z}} \times [E_{\rho mi}^*(\rho)\hat{\boldsymbol{\rho}} + E_{\phi mi}^*(\rho)\hat{\boldsymbol{\phi}}]$. The basis functions in region 1 and 3 are given by $\mathbf{H}_v^{(1,3)} = \mathbf{H}_{tpq}^{(1,3)}$. Once again, the overlap between testing functions and the incident field is contained in the vector

$$V_u^{(h0)} = \int_H \mathbf{E}_u \cdot \mathbf{H}^{(0)} \rho d\rho d\phi. \tag{4.61}$$

It remains to solve for the unknown coefficients contained in $\mathbf{A}$ and $\mathbf{B}$. We begin by solving for the waveguide mode coefficient vectors $\mathbf{C}^{(+)}$ and $\mathbf{C}^{(-)}$:

$$\mathbf{C}^{(+)} = \mathbf{M}^{(f)-1}(\mathbf{S}^{(e0)} + \mathbf{S}^{(h0)}) \tag{4.62}$$

$$\mathbf{C}^{(-)} = -\mathbf{Q}^{(mr)-1}\mathbf{Q}^{(pr)}\mathbf{C}^{(+)}. \tag{4.63}$$

The intermediate quantities are defined in the Appendix. The unknown vectors $\mathbf{A}$ and $\mathbf{B}$ are determined from $\mathbf{C}^{(+)}$ and $\mathbf{C}^{(-)}$:

$$\mathbf{A} = \mathbf{Z}^{(e1)-1}\left[-\mathbf{V}^{(e0)} + \mathbf{M}^{(e1)}\mathbf{D}^{(1)}\mathbf{C}^{(+)} + \mathbf{M}^{(e1)}\mathbf{D}^{(2)}\mathbf{C}^{(-)}\right] \tag{4.64}$$

$$\mathbf{B} = \mathbf{Z}^{(e2)-1}\left[\mathbf{M}^{(e2)}\mathbf{D}^{(2)}\mathbf{C}^{(+)} + \mathbf{M}^{(e2)}\mathbf{D}^{(1)}\mathbf{C}^{(-)}\right]. \tag{4.65}$$

Once $\mathbf{B}$ is known, the transmission through the film may be calculated.

4.6 Results

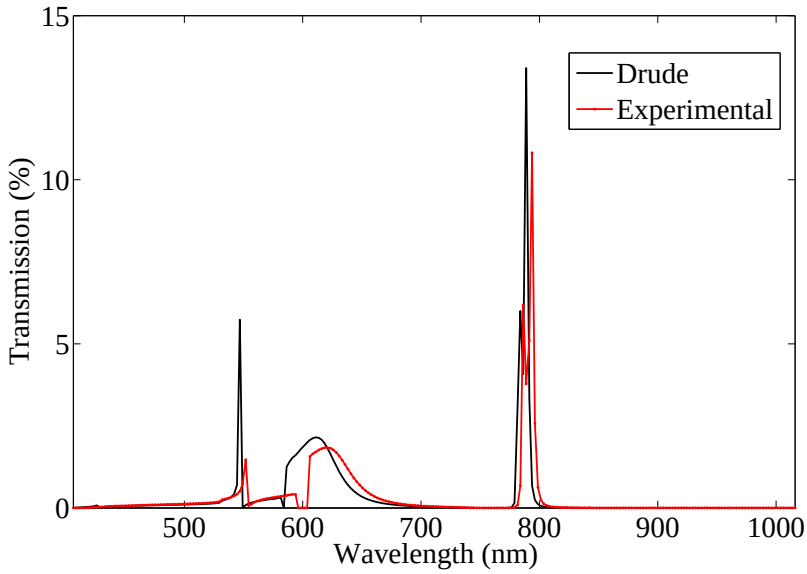

Figure 4.2 Theoretical transmission through a 320 nm thick silver film perforated by a square array of circular holes of radius 140 nm and lattice constant 750 nm at normal incidence. The transmission profile was calculated using the Drude model (black line) and experimental values (red dotted line) for the silver permittivity.

Before comparing the theoretical and experimental transmission data directly, I study the effect of two different models for the silver permittivity on the profile. Consider transmission through a 320 nm thick silver film perforated by a square array of circular holes of radius 140 nm and lattice constant 750 nm at normal incidence. Figure 4.2 shows the theoretical transmission profiles when both the Drude model and measured data are used for the silver permittivity. Note that the amplitude of the transmission peaks is slightly reduced when the experimental permittivities are used in the calculation. This may be understood by observing that the Drude model underestimates losses in the silver over optical wavelengths. One also observes a small shift in the position of the peaks with respect to wavelength.

Figure 4.3 shows the theoretical transmission profile for the same geometry. The holes cover only 11% of the area of the film, yet the peak transmission is nearly 15%, a transmission-to-area efficiency of roughly 130%. This is in excellent agreement with experimental data ([47],

Fig. 1). Martin-Moreno *et al.* further point out that single aperture theory (which assumes a PEC screen) predicts a transmission efficiency on the order of 1% in this frequency regime.

The theory presented here agrees well with the experimental peak transmission through a finite array of 21×21 circular holes.[47] Previous modal approaches significantly over-estimate the transmission around a wavelength of 800 nm, ranging from 43%[46] if an IBC is imposed on the upper and lower horizonatal surfaces only to 50%[47] for an infinite PEC array. Small variations in the finite array hole diameters may explain the broader peaks in the experimental data. However, the overestimation of peak transmission is related to the boundary condition on the hole wall.

The improved agreement between experiment and theory when an IBC is included in the hole may be attributed to a more realistic model of the fundamental mode. At optical wavelengths, the fundamental dominates the fields inside the hole. When an IBC is imposed on the hole wall, the fundamental is the hybrid HEM11 mode (Figures 4.4 and 4.5). Here the azimuthal number is one and we take the first eigenvalue. Both TM and TE potentials contribute to the fundamental under the IBC approximation. Notice that a significant tangential electric field exists on the surface of the hole at $\rho = a$ (Figures 4.4a,b and 4.5a,b). If the IBC is replaced with a PEC as in [46] and [47], the fields are squeezed to allow a null on the hole wall (Figures 4.4c,d and 4.5c,d). In order to compensate for this, Martin-Moreno *et al.* enlarge the hole by assuming an effective hole radius equal to the original value plus twice the skin depth.[46] Enlarging the hole extends the field past the true hole radius and neglects losses in the silver. Energy that should be absorbed leaks through and the transmission is overestimated.

Next I study the impact of film thickness, hole radius, lattice constant, and angle of incidence on the transmission profile for the purpose of identifying a mechanism for EOT. Surface plasma polaritons tied to the interface between a dielectric and a metal have been included in a possible mechanism.[47][48] While the exact role of surface waves in EOT has been a matter of debate, they help to explain the results reported herein. First, note that transmission through the film is a strong function of the film thickness (Figure 4.6). The transmission peaks are

associated with waves bound to the top and bottom surfaces. When the film is thin, coupling between the upper and lower surfaces is strong and two peaks at different wavelengths may be observed. As the film thickness increases, the coupling weakens and the peaks merge. The response for the 500 nm thick film is dominated by uncoupled surfaces waves.

Both the amplitude and position of the the transmission peaks are affected by the hole radius (Figure 4.7). Unsurprisingly, larger holes transmit more energy through the film. The peaks also shift towards longer wavelengths as the radius of the hole increases. This wavelength shift is related to the resonant character of the transmission process. The peaks occur for holes of a certain size relative to the wavelength. As the wavelength increases, this relative size remains roughly constant. The peak position increases to maintain the resonant ratio between hole radius and wavelength.

The position of the transmission peaks can largely be explained by the presence of surface plasmon polaritons. At the air-metal interface, the SPPs must satisfy conservation of momentum

$$\mathbf{k}_{sp} = \mathbf{k}_{0t} + i\mathbf{G_x} + j\mathbf{G_y} \tag{4.66}$$

where $\mathbf{k}_{0t}$ is the component of the incident wavevector that is parallel to the surface. The reciprocal vectors are determined by the lattice constants of the film

$$G_x = 2\pi/D_x \tag{4.67}$$

$$G_y = 2\pi/D_y. \tag{4.68}$$

The dispersion relationship for SPPs is given by

$$k_{sp} = \mathrm{Re}\left[\frac{\omega}{c}\sqrt{\frac{\epsilon_m\epsilon_d}{\epsilon_m+\epsilon_d}}\right] \tag{4.69}$$

where ϵ_m and ϵ_d are the permittivities of the metal and the surrounding medium, respectively.[45] Using equations (4.66) and (4.69), the wavelength of the first-order SPP at normal incidence may be determined

$$\lambda_{sp} = \mathrm{Re}\left[\sqrt{\frac{\epsilon_m\epsilon_d}{\epsilon_m+\epsilon_d}}\right] D_x. \tag{4.70}$$

Equation (4.70) shows the relationship between the lattice constant and the SPP wavelength. Therefore, the lattice constant significantly affects the transmission profile by determining the

wavelength at which the SPPs occur (Figure 4.8). The peaks consistently occur at a wavelength slightly greater than the lattice constant. The amplitude of the transmission peaks decreases as the lattice constant increases. For a constant hole radius, a smaller fraction of the film area is covered by the holes as the lattice constant increases and less energy is transmitted. However, the transmission-to-area efficiency is not constant with respect to lattice constant (Figure 4.9). For a lattice constant D=600 nm, 17% of the film area is covered by the holes. We observe a maximum transmission of approximately 57% for a transmission-to-area efficiency of roughy 335%. The efficiency decreases to 68% for a lattice constant of 800 nm. Smaller lattice constants appear to be more efficient than larger lattice constants. Surface waves again help to explain this trend. Martin-Moreno *et al.* identify modes supported by a single interface with parallel momentum $2\pi/D$, the so-called first-order surface plasma polariton.[47] As the lattice constant decreases, more parallel momentum is carried by the first-order SPP. The surface wave traps more energy that is funneled through the film by the fundamental mode.

Finally, consider the impact of angle of incidence on EOT. Figure 4.10 shows the polarization and angle of rotation for the incident field. The electric field is directed along the x-direction which is also the axis of rotation. Losses in the silver have been neglected to clarify the trend in Figure 4.11. At normal incidence, observe the characteristic peak around 800 nm. As the angle of incidence increases the peaks are significantly red-shifted. Figure 4.12 shows the transmission profile as a function of incident angle over a larger range of wavelengths. As the angle of incidence increases from normal, the single peak splits into two peaks that move in opposite directions. Martin-Moreno *et al.* note that these peaks occur at wavelengths associated with bound surface modes.[39]

4.7 Conclusions

A mode-matching solution to plane wave scattering by a silver film perforated by an infinite array of circular holes has been presented. Impedance boundary conditions have been imposed on all surfaces. The results predict a peak transmission value that is in good agreement with experiment. Extraordinary optical transmission has been studied as a function of film

thickness, hole radius, and lattice constant. The transmission profile position, shape, and amplitude are strong functions of film thickness, hole radius, and lattice constant. The coupling between modes bound to the upper and lower surfaces is strongly affected by film thickness. The resonant nature of the EOT process dictates that transmission peaks occur for holes of a roughly constant electrical size. Small lattice constants transmit energy more efficiently than larger ones for the film under study. At angles of incidence greater than zero degrees the single transmission peak splits into two peaks. The results support the inclusion of surface waves in the mechanism for EOT.

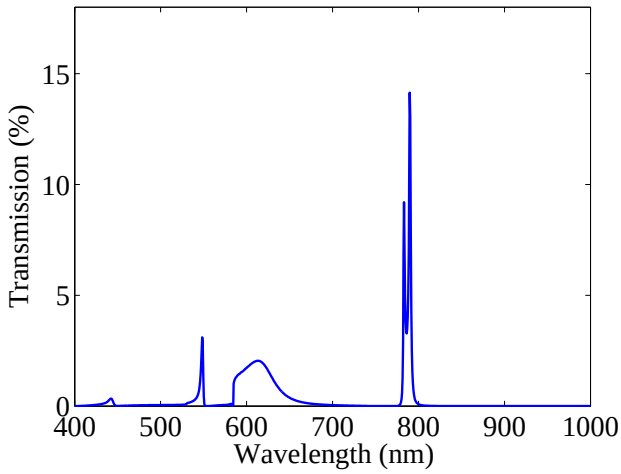

(a)

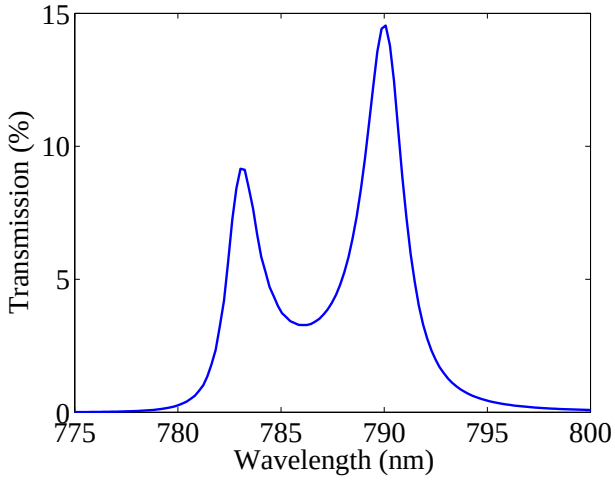

(b)

Figure 4.3 Theoretical extraordinary transmission through a 320 nm thick silver film perforated by an array of circular holes of radius 140 nm and lattice constant 750 nm at normal incidence from 400 to 1000 nm(a) and from 775 to 800 nm(b).

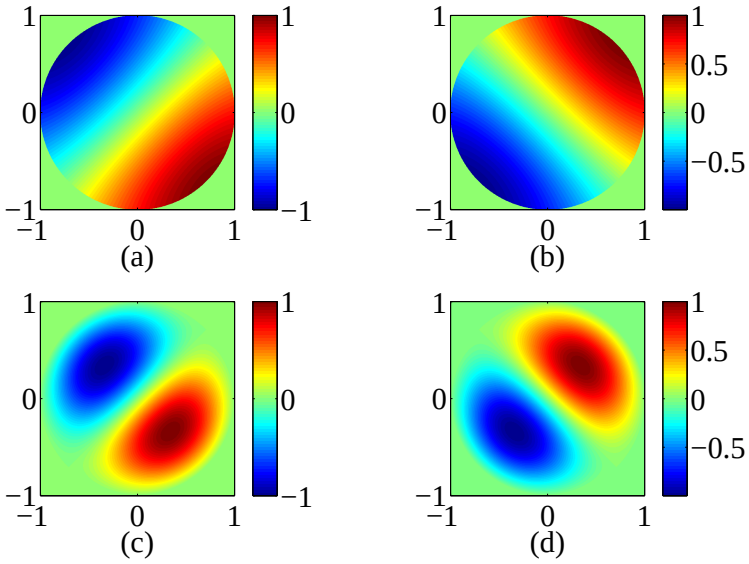

Figure 4.4 Normalized z-component of the electric field for the fundamental mode at a wavelength of 790 nm. The x and y-axes have been normalized by the hole radius. The panels show the real(a) and imaginary(b) parts of the field for the fundamental hybrid HEM11 mode used with an IBC on the hole wall. The remaining panels show the real(c) and imaginary(d) parts of the field for the fundamental TM11 mode used with a PEC boundary condition on the hole wall.

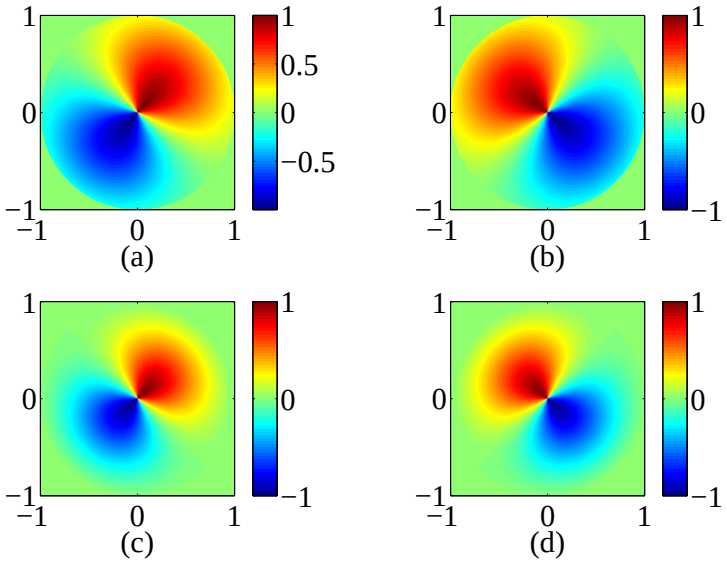

Figure 4.5 Normalized ϕ-component of the electric field for the fundamental mode at a wavelength of 790 nm. The x and y-axes have been normalized by the hole radius. The panels show the real(a) and imaginary(b) parts of the field for the fundamental hybrid HEM11 mode used with an IBC on the hole wall. The remaining panels show the real(c) and imaginary(d) parts of the field for the fundamental TM11 mode used with a PEC boundary condition on the hole wall.

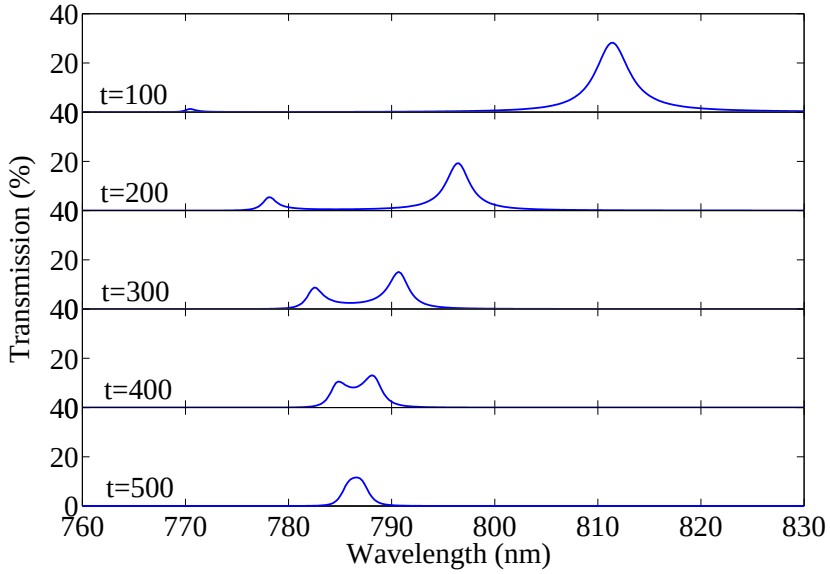

Figure 4.6 Theoretical transmission for the film thicknesses listed in the panel.

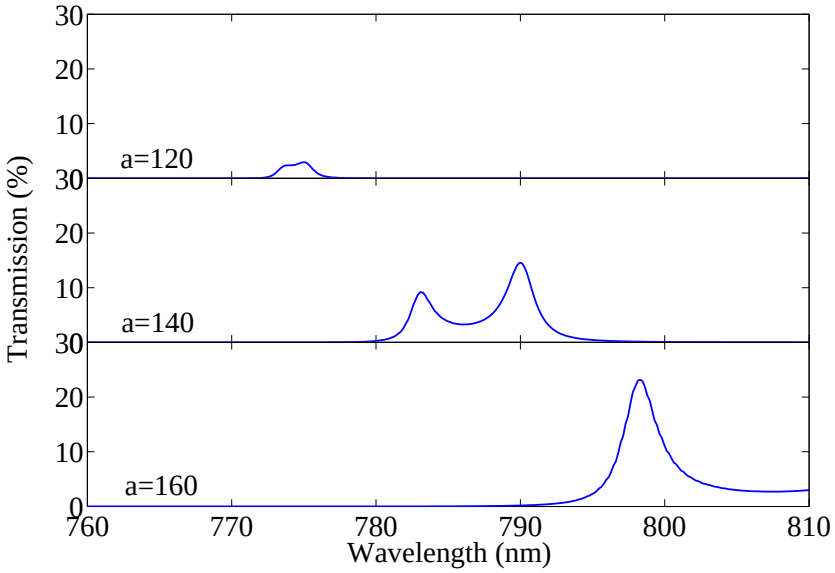

Figure 4.7 Theoretical transmission for the hole radii listed in the panel for a 320 nm thick film with lattice constant 750 nm.

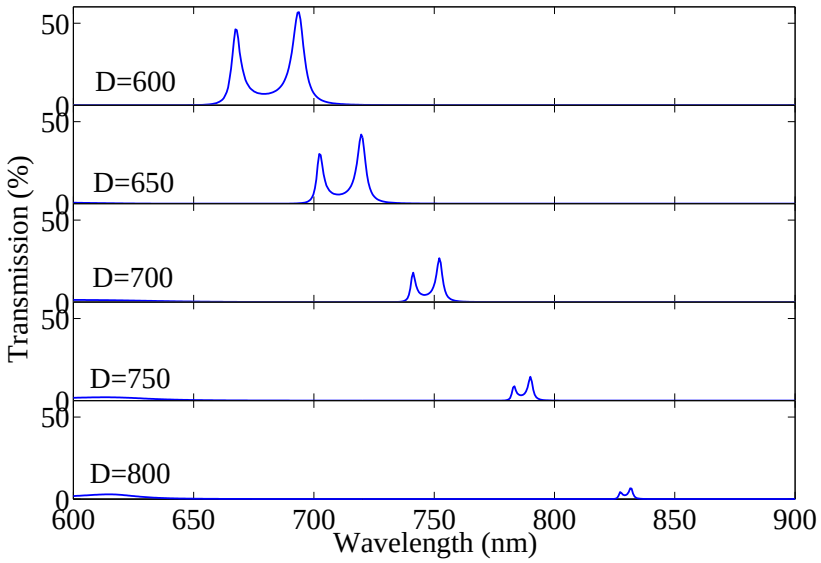

Figure 4.8 Theoretical transmission for the lattice constants listed in the panel for a 320 nm thick film with hole radius of 140 nm.

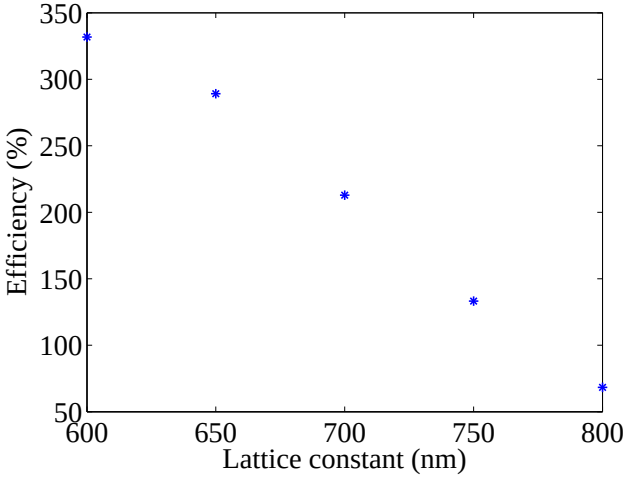

Figure 4.9 Theoretical transmission-to-area efficiency as a function of lattice constant.

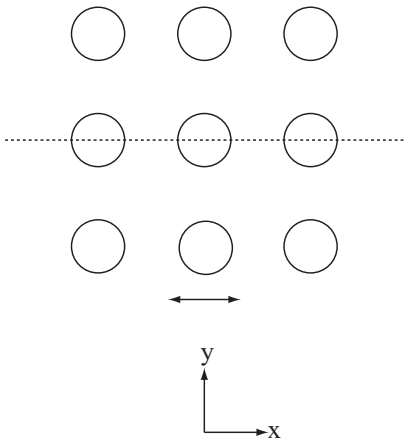

Figure 4.10 Polarization (double arrows) and axis of rotation (dashed line) for incident field.

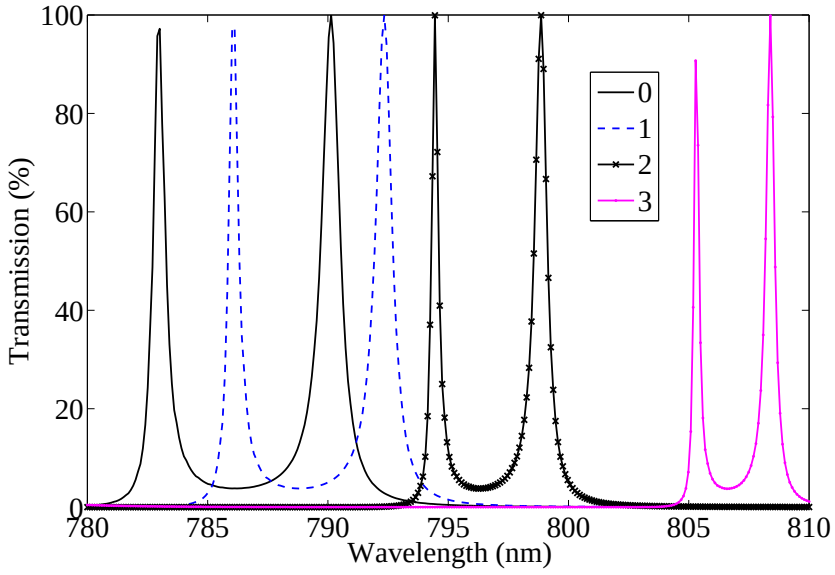

Figure 4.11 Transmission for the incident angles (in degrees) listed in the panel.

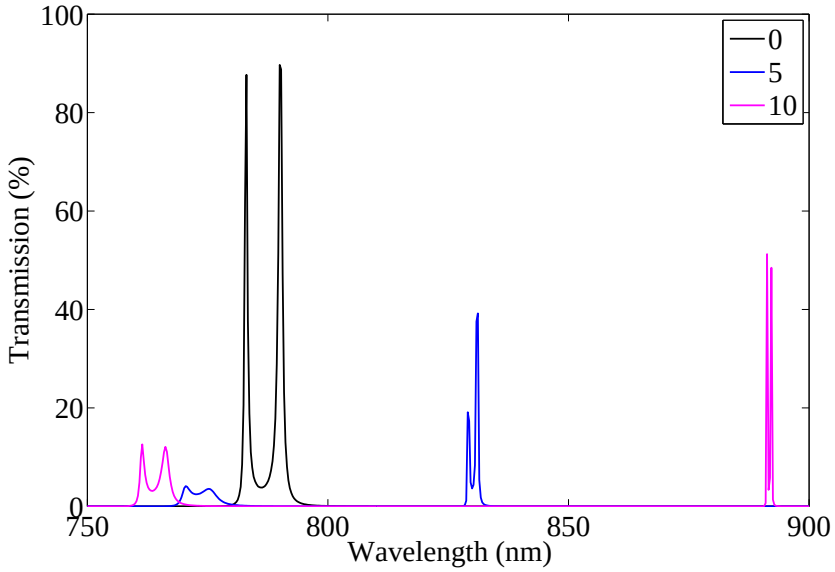

Figure 4.12 Transmission for the incident angles (in degrees) listed in the panel.

APPENDIX A Fourier-Bessel series representation of the TM Green's functions

In this section, we propose a Fourier-Bessel series representation of the TM Green's function for the hollow circular and circular sectoral waveguides. We begin with the analysis of the hollow circular waveguide.

Hollow Circular Waveguide

We seek a solution to

$$(\nabla^2 + k^2)g^{(tm)}(\rho, \rho_s, \phi - \phi_s, z - z_s) = -\delta(\rho - \rho_s)\delta(\phi - \phi_s)\delta(z - z_s)/\rho \tag{A.1}$$

where $g^{(tm)}(a, \rho_s, \phi - \phi_s, z - z_s) = 0$. The following standard completeness relations are used in (A.1):

$$\delta(\phi - \phi_s) = \frac{1}{2\pi} \sum_{m=-\infty}^{\infty} \exp[-\jmath m(\phi - \phi_s)] \tag{A.2}$$

and

$$\delta(z - z_s) = \frac{1}{2\pi} \int_{-\infty}^{\infty} \exp[\jmath\beta(z - z_s)]d\beta. \tag{A.3}$$

In this case, we also take advantage of the completeness relation for Bessel functions[2]:

$$\frac{\delta(\rho - \rho_s)}{\rho_s} = \sum_{i=1}^{\infty} \frac{1}{c_{mi}^2} \mathrm{J}_m(\gamma_{mi}\rho)\mathrm{J}_m(\gamma_{mi}\rho_s) \tag{A.4}$$

where

$$c_{mi}^2 = \int_0^a \mathrm{J}_m^2(\gamma_{mi}\rho)\rho d\rho = \frac{a^2}{2}\mathrm{J}_{m+1}^2(\gamma_{mi}a) \tag{A.5}$$

and $\gamma_{mi} = p_{mi}/a$ where p_{mi} the ith zero of the Bessel function of order m. The Green's function may be expanded in a Fourier series in the azimuthal direction

$$g^{(tm)}(\rho, \rho_s, \phi - \phi_s, z - z_s) = \sum_{m=-\infty}^{\infty} g_m^{(tm)}(\rho, \rho_s, z - z_s) \exp[-\jmath m(\phi - \phi_s)]. \tag{A.6}$$

The unknown coefficients are written as an inverse Fourier transform thus

$$g_m^{(tm)}(\rho, \rho_s, z - z_s) = \frac{1}{2\pi} \int_{-\infty}^{\infty} \widetilde{\psi}_m(\rho, \rho_s) \exp[\jmath\beta(z - z_s)] d\beta. \tag{A.7}$$

By completeness, the radial function may be further expanded in terms of Eigenfunctions

$$\widetilde{g}_m^{(tm)}(\rho, \rho_s) = \sum_{i=1}^{\infty} A_{mi}(\beta) \frac{1}{c_{mi}^2} \mathrm{J}_m(\gamma_{mi}\rho) \mathrm{J}_m(\gamma_{mi}\rho_s). \tag{A.8}$$

Making the appropriate substitutions in (A.1) yields

$$\begin{aligned} &\left\{\mathcal{L}^2 - \gamma^2\right\} \sum_{i=1}^{\infty} A_{mi}(\beta) \frac{1}{c_{mi}^2} \mathrm{J}_m(\gamma_{mi}\rho) \mathrm{J}_m(\gamma_{mi}\rho_s) = \\ &\frac{1}{2\pi} \sum_{i=1}^{\infty} \frac{1}{c_{mi}^2} \mathrm{J}_m(\gamma_{mi}\rho) \mathrm{J}_m(\gamma_{mi}\rho_s) \end{aligned} \tag{A.9}$$

where

$$\mathcal{L}^2 = -\frac{1}{\rho} \frac{\partial}{\partial \rho} \left(\rho \frac{\partial}{\partial \rho} \right) + \frac{m^2}{\rho^2}. \tag{A.10}$$

By definition of an Eigenfunction,

$$\mathcal{L}^2 \mathrm{J}_m(\gamma_{mi}\rho) = \gamma_{mi}^2 \mathrm{J}_m(\gamma_{mi}\rho). \tag{A.11}$$

Using (A.11) in (A.9)

$$\begin{aligned} &\left\{\gamma_{mi}^2 - \gamma^2\right\} \sum_{i=1}^{\infty} A_{mi}(\beta) \frac{1}{c_{mi}^2} \mathrm{J}_m(\gamma_{mi}\rho) \mathrm{J}_m(\gamma_{mi}\rho_s) = \\ &\frac{1}{2\pi} \sum_{i=1}^{\infty} \frac{1}{c_{mi}^2} \mathrm{J}_m(\gamma_{mi}\rho) \mathrm{J}_m(\gamma_{mi}\rho_s). \end{aligned} \tag{A.12}$$

The orthogonality of the Bessel function implies that

$$A_{mi}(\beta) = \frac{1}{\gamma_{mi}^2 - \gamma^2}. \tag{A.13}$$

Therefore, the Green's function for the hollow circular waveguide takes the form

$$\begin{aligned} g^{(tm)}(\rho, \rho_s, \phi - \phi_s, z - z_s) = \frac{1}{(2\pi)^2} \sum_{m=-\infty}^{\infty} \sum_{i=1}^{\infty} \frac{1}{c_{mi}^2} \mathrm{J}_m(\gamma_{mi}\rho_s) \exp[-\jmath m(\phi - \phi_s)] \cdot \\ \int_{-\infty}^{\infty} \frac{\mathrm{J}_m(\gamma_{mi}\rho)}{\gamma_{mi}^2 - \gamma^2} \exp[\jmath\beta(z - z_s)] d\beta. \end{aligned} \tag{A.14}$$

Using the definition of γ, equation (A.14) may be expressed as

$$g^{(tm)}(\rho,\rho_s,\phi-\phi_s,z-z_s)=\frac{1}{(2\pi)^2}\sum_{m=-\infty}^{\infty}\sum_{i=1}^{\infty}\frac{1}{c_{mi}^2}\mathrm{J}_m(\gamma_{mi}\rho_s)\exp[-\jmath m(\phi-\phi_s)]\cdot \int_{-\infty}^{\infty}\frac{\mathrm{J}_m(\gamma_{mi}\rho)}{\gamma_{mi}^2-k^2+\beta^2}\exp[\jmath\beta(z-z_s)]d\beta. \tag{A.15}$$

The denominator of the integrand may be factored thus

$$g^{(tm)}(\rho,\rho_s,\phi-\phi_s,z-z_s)=\frac{1}{(2\pi)^2}\sum_{m=-\infty}^{\infty}\sum_{i=1}^{\infty}\frac{1}{c_{mi}^2}\mathrm{J}_m(\gamma_{mi}\rho_s)\exp[-\jmath m(\phi-\phi_s)]\cdot \int_{-\infty}^{\infty}\frac{\mathrm{J}_m(\gamma_{mi}\rho)\exp[\jmath\beta(z-z_s)]}{\left(\beta-\sqrt{k^2-\gamma_{mi}^2}\right)\left(\beta+\sqrt{k^2-\gamma_{mi}^2}\right)}d\beta. \tag{A.16}$$

As no branch cut occurs in the integrand of (A.16), the integral may be evaluated via the residue theorem[14]

$$g^{(tm)}(\rho,\rho_s,\phi-\phi_s,z-z_s)=\sum_{m=-\infty}^{\infty}\sum_{i=1}^{\infty}\frac{u_{mi}}{c_{mi}^2}\mathrm{J}_m(\gamma_{mi}\rho)\mathrm{J}_m(\gamma_{mi}\rho_s)\exp[-\jmath m(\phi-\phi_s)]\cdot \frac{\exp\left[\jmath\sqrt{k^2-\gamma_{mi}^2}(z-z_s)\right]}{\sqrt{k^2-\gamma_{mi}^2}} \tag{A.17}$$

where

$$u_{mi}=\begin{cases}\frac{\jmath}{8\pi} & \gamma_{mi}<k\\ \\ \frac{\jmath}{4\pi} & \gamma_{mi}>k.\end{cases} \tag{A.18}$$

Circular sectoral waveguide

The derivation for the circular sectoral waveguide is similar to that of the previous section. We employ the direct Ohm-Raleigh method. The governing equation is again

$$(\nabla^2+k^2)G^{(tm)}(\rho,\rho_s,\phi-\phi_s,z-z_s)=-\delta(\rho-\rho_s)\delta(\phi-\phi_s)\delta(z-z_s)/\rho. \tag{A.19}$$

We have Dirichlet boundary conditions on the surface of the wedge $G^{(tm)}(\rho,\rho_s,0-\phi_s,z-z_s)=G^{(tm)}(\rho,\rho_s,\phi_0-\phi_s,z-z_s)=0$ and on the walls of the guide $G^{(tm)}(a,\rho_s,\phi-\phi_s,z-z_s)=0$. Again, we choose to solve (A.19) directly. To this end, we propose the following Eigenfunction

expansion of the Green's function

$$G^{(tm)}(\rho,\rho_s,\phi-\phi_s,z-z_s)=\frac{1}{\phi_0\pi}\sum_{m=1}^{\infty}\sum_{i=1}^{\infty}\frac{1}{c_{mi}^2}\mathrm{J}_\mu(\gamma_{mi}\rho_s)\sin(\mu\phi)\sin(\mu\phi_s)\cdot \int_{-\infty}^{\infty}\frac{\mathrm{J}_\mu(\gamma_{mi}\rho)}{\gamma_{mi}^2-\gamma^2}\exp[\jmath\beta(z-z_s)]d\beta. \tag{A.20}$$

Here $\gamma_{mi}=p_{\mu i}/a$ where $p_{\mu i}$ is the ith zero of the Bessel function of order $\mu=m\pi/\phi_0$ and [13]

$$c_{mi}^2=\int_0^a \mathrm{J}_\mu^2(\gamma_{mi}\rho)\rho d\rho=\frac{a^2}{2}\left[\mathrm{J}'_m(\gamma_{mi}a)\right]^2. \tag{A.21}$$

As mentioned above, the TM potential satisfies a Dirichlet boundary condition on the surface of the wedge. Therefore, the azimuthal basis is chosen to be Sine functions. Again, the integrand in (A.20) may be factored

$$G^{(tm)}(\rho,\rho_s,\phi-\phi_s,z-z_s)=\frac{1}{\phi_0\pi}\sum_{m=1}^{\infty}\sum_{i=1}^{\infty}\frac{1}{c_{mi}^2}\mathrm{J}_\mu(\gamma_{mi}\rho_s)\sin(\mu\phi)\sin(\mu\phi_s)\cdot \int_{-\infty}^{\infty}\frac{\mathrm{J}_\mu(\gamma_{mi}\rho)\exp[\jmath\beta(z-z_s)]}{\left(\beta-\sqrt{k^2-\gamma_{mi}^2}\right)\left(\beta+\sqrt{k^2-\gamma_{mi}^2}\right)}d\beta. \tag{A.22}$$

The residue theorem implies that

$$G^{(tm)}(\rho,\rho_s,\phi-\phi_s,z-z_s)=\sum_{m=1}^{\infty}\sum_{i=1}^{\infty}\frac{d_{mi}}{c_{mi}^2}\mathrm{J}_\mu(\gamma_{mi}\rho)\mathrm{J}_\mu(\gamma_{mi}\rho_s)\sin(\mu\phi)\sin(\mu\phi_s)\cdot \frac{\exp\left[\jmath\sqrt{k^2-\gamma_{mi}^2}(z-z_s)\right]}{\sqrt{k^2-\gamma_{mi}^2}} \tag{A.23}$$

where

$$d_{mi}=\begin{cases}\frac{\jmath}{2\phi_0} & \gamma_{mi}<k\\ \frac{\jmath}{\phi_0} & \gamma_{mi}>k.\end{cases} \tag{A.24}$$

APPENDIX B Plasma matrix definitions

Standing Wave Definitions

We begin with the x-component of the electric field. The orthogonality of the Fourier series over the surface of the electrode leads to two families of solutions. The coefficients a_{mn}, d_{mn}, p_{mn}, and s_{mn} are coupled by the boundary conditions.

$$\begin{aligned} &- mL_y\beta_1 \sin(\beta_1 s)a_{mn} - \jmath\omega\mu_1 nL_x \sin(\beta_1 s)d_{mn} = \\ &mL_y\beta_2 \sin(\beta_2 t/2)p_{mn} - \jmath\omega\mu_2 nL_x \sin(\beta_2 t/2)s_{mn}. \end{aligned} \tag{B.1}$$

Continuity of the y-component of the electric field implies

$$\begin{aligned} &- nL_x\beta_1 \sin(\beta_1 s)a_{mn} + \jmath\omega\mu_1 mL_y \sin(\beta_1 s)d_{mn} = \\ &nL_x\beta_2 \sin(\beta_2 t/2)p_{mn} + \jmath\omega\mu_2 mL_y \sin(\beta_2 t/2)s_{mn}. \end{aligned} \tag{B.2}$$

Continuity of the tangential magnetic field is ensured by

$$\begin{aligned} &- mL_y\beta_1 \cos(\beta_1 s)d_{mn} + \jmath\omega\epsilon_1 nL_x \cos(\beta_1 s)a_{mn} \\ &+ \jmath\omega\epsilon_1 nL_x a_{mn}^{(0)} = \\ &mL_y\beta_2 \cos(\beta_2 t/2)s_{mn} - \jmath\omega\epsilon_2 nL_x \cos(\beta_2 t/2)p_{mn} \end{aligned} \tag{B.3}$$

$$\begin{aligned} &\jmath nL_x\beta_1 \cos(\beta_1 s)d_{mn} - \jmath\omega\epsilon_1 mL_y \cos(\beta_1 s)a_{mn} \\ &+ \jmath\omega\epsilon_1 mL_y a_{mn}^{(0)} = \\ &nL_x\beta_2 \cos(\beta_2 t/2)s_{mn} + \jmath\omega\epsilon_2 mL_y \cos(\beta_2 t/2)p_{mn}. \end{aligned} \tag{B.4}$$

These equations represent a system of four equations and four unknowns

$$\mathbf{ZC_d} = \mathbf{A_0} \tag{B.5}$$

where $\mathbf{C_d} = \begin{bmatrix} a_{mn} \\ d_{mn} \\ p_{mn} \\ s_{mn} \end{bmatrix}$ is a vector of unknown coefficients. The impedance matrix $\mathbf{Z}$ and vector $\mathbf{A_0}$ are defined thus:

$$\mathbf{Z} = \begin{bmatrix} \jmath\omega\epsilon_1 nL_x \cos(\beta_1 s) & -mL_y\beta_1 \cos(\beta_1 s) & \jmath\omega\epsilon_2 nL_x \cos(\beta_2 t/2) & -mL_y\beta_2 \cos(\beta_2 t/2) \\ -\jmath\omega\epsilon_1 mL_y \cos(\beta_1 s) & \jmath nL_x\beta_1 \cos(\beta_1 s) & -\jmath\omega\epsilon_2 mL_y \cos(\beta_2 t/2) & -nL_x\beta_2 \cos(\beta_2 t/2) \\ -mL_y\beta_1 \sin(\beta_1 s) & -\jmath\omega\mu_1 nL_x \sin(\beta_1 s) & -mL_y\beta_2 \sin(\beta_2 t/2) & \jmath\omega\mu_2 nL_x \sin(\beta_2 t/2) \\ -nL_x\beta_1 \sin(\beta_1 s) & \jmath\omega\mu_1 mL_y \sin(\beta_1 s) & -nL_x\beta_2 \sin(\beta_2 t/2) & -\jmath\omega\mu_2 mL_y \sin(\beta_2 t/2) \end{bmatrix} \tag{B.6}$$

and

$$\mathbf{A_0} = \begin{bmatrix} -\jmath\omega\epsilon_1 nL_x a_{mn}^{(0)} \\ \jmath\omega\epsilon_1 mL_y a_{mn}^{(0)} \\ 0 \\ 0 \end{bmatrix}. \tag{B.7}$$

The coefficients b_{mn}, c_{mn}, q_{mn}, and r_{mn} satisfy a similar system of equations:

$$\mathbf{ZC_{vn}} = \mathbf{D_0} \tag{B.8}$$

where $\mathbf{C_{vn}} = \begin{bmatrix} b_{mn} \\ c_{mn} \\ q_{mn} \\ r_{mn} \end{bmatrix}$ is a vector of unknown coefficients and $\mathbf{D_0} = \begin{bmatrix} -\jmath\omega\epsilon_1 nL_x d_{mn}^{(0)} \\ \jmath\omega\epsilon_1 mL_y d_{mn}^{(0)} \\ 0 \\ 0 \end{bmatrix}$.

Edge Wave Definitions

The matrix equations for the edge wave coefficients are given by $\mathbf{Z_{mn}C_{mn}} = \mathbf{V_{mn}^{(c)}}$ and $\mathbf{Z_{mn}S_{mn}} = \mathbf{V_{mn}^{(s)}}$. The matrix and vectors are defined thus

$$\mathbf{Z_{mn}} = \begin{bmatrix} 0 & k^2 \exp(\beta_n L_x/2) & k^2 \exp(-\beta_n L_x/2) & -k^2 D_{mn} \\ -k^2 D_{mn} & k^2 \exp(-\beta_n L_x/2) & k^2 \exp(\beta_n L_x/2) & 0 \\ 0 & -\beta_n \exp(\beta_n L_x/2) & \beta_n \exp(-\beta_n L_x/2) & -\jmath E_{mn} \\ \jmath E_{mn} & -\beta_n \exp(-\beta_n L_x/2) & \beta_n \exp(\beta_n L_x/2) & 0.0 \end{bmatrix} \tag{B.9}$$

where $D_{mn} = 1 + c_{mn}^{(-)}$ and $E_{mn} = \jmath\beta_n \left[1 - c_{mn}^{(-)}\right]$,

$$\mathbf{C_{mn}} = \begin{bmatrix} a_{mn}^{(l+)} \\ c_{mn}^{(x+)} \\ c_{mn}^{(x-)} \\ a_{mn}^{(r+)} \end{bmatrix}, \tag{B.10}$$

$$\mathbf{S_{mn}} = \begin{bmatrix} d_{mn}^{(l+)} \\ s_{mn}^{(x+)} \\ s_{mn}^{(x-)} \\ d_{mn}^{(r+)} \end{bmatrix}, \tag{B.11}$$

$$\mathbf{V_{mn}^{(c)}} = \begin{bmatrix} -k^2 \cos(m\pi) \left[a_{mn}^{(0)} + a_{mn}\right] \\ -k^2 \left[a_{mn}^{(0)} + a_{mn}\right] \\ 0 \\ 0 \end{bmatrix}, \tag{B.12}$$

and

$$\mathbf{V_{mn}^{(s)}} = \begin{bmatrix} 0 \\ 0 \\ -\jmath m\pi/L_x \cos(m\pi) \left[d_{mn}^{(0)} + d_{mn}\right] \\ -\jmath m\pi/L_x \left[d_{mn}^{(0)} + d_{mn}\right] \end{bmatrix}. \tag{B.13}$$

APPENDIX C Intermediate matrix definitions

$$\mathbf{P}^{(p)} = \mathbf{M}^{(h1)}\mathbf{Z}^{(e1)-1}\mathbf{M}^{(e1)}\mathbf{D}^{(1)} - \mathbf{D}^{(1)} \tag{C.1}$$

$$\mathbf{P}^{(m)} = \mathbf{M}^{(h1)}\mathbf{Z}^{(e1)-1}\mathbf{M}^{(e1)}\mathbf{D}^{(2)} + \mathbf{D}^{(2)} \tag{C.2}$$

$$\mathbf{R}^{(e0)} = \mathbf{M}^{(h1)}\mathbf{Z}^{(e1)-1}\mathbf{V}^{(e0)} \tag{C.3}$$

$$\mathbf{R}^{(h0)} = \mathbf{V}^{(h0)} \tag{C.4}$$

$$\mathbf{Q}^{(p)} = \mathbf{M}^{(h2)}\mathbf{Z}^{(e2)-1}\mathbf{M}^{(e2)}\mathbf{D}^{(2)} - \mathbf{D}^{(2)} \tag{C.5}$$

$$\mathbf{Q}^{(m)} = \mathbf{M}^{(h2)}\mathbf{Z}^{(e2)-1}\mathbf{M}^{(e2)}\mathbf{D}^{(1)} + \mathbf{D}^{(1)} \tag{C.6}$$

The dimension of these matrices is N, the number of Floquet modes used in the series. Often more modes are needed to represent the fields above and below the film than inside the hole. This results in nonsquare matrices upon testing. In order to solve the system, we reduce the dimensionality of the larger matrices:

$$\mathbf{P}^{(pr)} = \mathbf{P}^{(p)}_{1:N_h,1:N_h} \tag{C.7}$$

$$\mathbf{P}^{(mr)} = \mathbf{P}^{(m)}_{1:N_h,1:N_h} \tag{C.8}$$

$$\mathbf{Q}^{(pr)} = \mathbf{Q}^{(p)}_{1:N_h,1:N_h} \tag{C.9}$$

$$\mathbf{Q}^{(mr)} = \mathbf{Q}^{(m)}_{1:N_h,1:N_h}. \tag{C.10}$$

Here N_h is the number of waveguide modes in the hole region.

$$\mathbf{M}^{(f)} = \mathbf{Q}^{(pr)} - \mathbf{Q}^{(mr)}\mathbf{P}^{(mr)-1}\mathbf{P}^{(pr)} \tag{C.11}$$

$$\mathbf{S}^{(e0)} = -\mathbf{Q}^{(mr)}\mathbf{P}^{(mr)-1}\mathbf{R}^{(e0)} \tag{C.12}$$

$$\mathbf{S}^{(h0)} = \mathbf{Q}^{(mr)}\mathbf{P}^{(mr)-1}\mathbf{R}^{(h0)} \tag{C.13}$$

BIBLIOGRAPHY

[1] Edward J. Rothwell and Michael J. Cloud, *Electromagnetics*, (CRC Press LLC, Boca Raton, FL, 2001).

[2] George W. Hanson and Alexander B. Yakovlev, *Operator Theory for Electromagnetics* (Springer, New York, 2002).

[3] John K. Hunter and Bruno Nachtergaele, *Applied Analysis* (World Scientific, Hackensack, NJ, 2001).

[4] L.B. Felsen and N. Marcuvitz, *Radiation and Scattering of Waves* (IEEE Press, Piscataway, New Jersey, 1994).

[5] James R. Wait, *Electromagnetic radiation from cylindrical structures* (Peter Peregrinus Ltd., London, UK, 1988).

[6] B.A. Mishustin, A representation of the Green's function for an infinite perfectly conducting wedge, *Radiophysics and Quantum Electronics*, **34**, 82-85, (1991).

[7] C.T. Tai, *Dyadic Greens Functions in Electromagnetic Theory* (IEEE Press, Piscataway, New Jersey, 2nd Edition 1994).

[8] T.P. Theodoulidis, Model of ferrite-cored probes for eddy current nondestructive evaluation, *Journal of Applied Physics*, **93**, 3071-3078, (2003).

[9] H. Sun, J.R. Bowler, and T.P. Theodoulidis, Eddy currents induced in a finite length layered rod by a coaxial coil, *IEEE Trans. on Magnetics*, **41**, No. 9, 2455-2461, (2003).

[10] Y. Li, G.Y. Tian, and A. Simm, Fast analytical modelling for pulsed eddy current evaluation, *NDT & E International*, **41**, Issue 9, 477-483, (2008).

[11] T.P. Theodoulidis and J.R. Bowler, Eddy current coil interaction with a right-angled conductive wedge, *Proceedings of the Royal Society of London: Series A*, **461**, No. 2062, 3123-3129, (2005).

[12] J.A. Stratton, *Electromagnetic Theory*, (McGraw-Hill, New York, 1941).

[13] A. Gray and G.B. Mathews, *A Treatise on Bessel Functions and Their Applications to Physics*, (Macmillan and Co., London, 2nd Edition 1922).

[14] P. Henrici, *Applied and Computational Complex Analysis: Vol. I* (Wiley, New York, 1988).

[15] K. Yasumoto, *Electromagnetic Theory and Applications for Photonic Crystals* (CRC Press LLC, Boca Raton, FL, 2006).

[16] I.S. Gradshteyn and I.M. Ryzhik, *Table of Integrals, Series, and Products*, (Academic Press, London, 7th Edition 2007).

[17] S.K. Burke, Impedance of a horizontal coil above a conducting half-space, *J. Phys. D: Appl. Phys.*, **19**, 1159-1173, (1986).

[18] L. Sansonnens, A. Pletzer, D. Magni, A.A. Howling, Ch. Hollenstein, and J.P.M. Schmitt, *Plasma Sources Sci. T.*, **6**, 170-178, (1997).

[19] L. Sansonnens, *J. Appl. Phys.*, **97**, 063304, (2005).

[20] Z. Chen, S. Rauf, and K. Collins, *J. Appl. Phys.*, **108**, 073301, (2010).

[21] M.A. Lieberman, J.P. Booth, P. Chabert, J.M. Rax and M.M. Turner, *Plasma Sources Sci. T.*, **11**, 283-293, (2002).

[22] P. Chabert, J.L. Raimbault, J.M. Rax, and M.A. Lieberman, *Phys. Plasmas*, **11**, 1775 (2004).

[23] L. Sansonnens and J. Schmitt, *Appl. Phys. Lett.*, **82**, 182 (2003).

[24] P. Chabert, J.L. Raimbault, J.M. Rax, and A. Perret, *Phys. Plasmas*, **11**, 4081 (2004).

[25] L. Sansonnens, A.A. Howling and Ch. Hollenstein, *Plasma Sources Sci. T.*, **15**, 302-313, (2006).

[26] P. Drude, *Ann. Phys.*, **306**, 566-613, (1900).

[27] TDK, TDK Corporation, www.tdk.com, (2012).

[28] J.B. Pendry, Playing Tricks with Light, *Science*, **285**, 1687, (1999).

[29] J.R. Krenn *et al.*, Squeezing the Optical Near-Field Zone by Plasmon Coupling of Metallic Nanoparticles, *Phys. Rev. Lett.*, **82**, 2590, (1999).

[30] J.R. Krenn *et al.* Non-diffraction limited light transport by gold nanowires, *Europhys. Lett.*, **60(5)**, 663669, (2001).

[31] B. Lamprecht *et al.*, Surface plasmon propagation in microscale metal stripes, *Appl. Phys. Lett.*, **79(1)**, 5153, (2001).

[32] S.A. Maier *et al.*, Local detection of electromagnetic energy transport below the diffraction limit in metal nanoparticle plasmon waveguides, *Nature Materials*, **2**, 229-232, (2003).

[33] R. Zia *et al.*, Geometries and materials for subwavelength surface plasmon modes, *J. Opt. Soc. Am. A*, **21(12)**, 2442, (2005).

[34] T.W. Ebbesen, H.J. Lezec, H.F. Ghaemi, T. Thio, and P.A. Wolff, Extraordinary optical transmission through sub-wavelength hole arrays, *Nature*, **391**, 667-669, (1998).

[35] H.A. Bethe, Theory of Diffraction by Small Holes, *Phys. Rev.*, **66**, 163, (1944).

[36] F.I. Baida and D. Van Labeke, Three-dimensional structures for enhanced transmission through a metallic film: Annular aperture arrays, *Phys. Rev. B*, **67**, 155314, (2003).

[37] Z. Li and L. Lin, Photonic band structures solved by a plane-wave-based transfer-matrix method, *Phys. Rev. E*, **67**, 046607, (2003).

[38] R. Biswas *et al.*, Theory of subwavelength hole arrays coupled with photonic crystals for extraordinary thermal emission, *Phys. Rev. B*, **74**, 045106, (2006).

[39] L. Martin-Moreno and F.J. Garcia-Vidal, Minimal model for optical transmission through holey metal films, *J. Phys.: Condens. Matter*, **20**, 304214, (2008).

[40] F. de Leon-Perez, G. Brucoli, F.J. Garcia-Vidal, and L. Martin-Moreno, Theory on the scattering of light and surface plasmon polaritons by arrays of holes and dimples in a metal film, *New Journal of Physics*, **10**, 105017, (2008).

[41] M. Zhang, C. Huang, G. Huang, and Y. Zhu, "Theory of extraordinary light transmission through sub-wavelength circular hole arrays," Journal of Optics, **12**, 015004 (2010).

[42] C. Huang, Q. Wang, and Y. Zhu, "Dual effect of surface plasmons in light transmission through perforated metal films," Physical Review B, **75**, 245421 (2007).

[43] Sergei Tretyakov, *Analytical Modeling in Applied Electromagnetics*, (Artech House, Inc., Norwood, MA, 2003).

[44] J. Parsons, E. Hendry, B. Augui, W. L. Barnes, and J. R. Sambles, "Localised modes of sub-wavelength hole arrays in thin metal films," **6988**, 69880 (2008).

[45] H. Raether, *Surface Plasmons*, Springer-Verlag, New York (1988).

[46] L. Martin-Moreno and F.J. Garcia-Vidal, Optical transmission through circular hole arrays in optically thick metal films, *Optics Express*, **12**, 3619, (2004).

[47] L. Martin-Moreno, F.J. Garcia-Vidal, H.J. Lezec, K.M. Pellerin, T. Thio, J.B. Pendry, and T.W. Ebbesen, Theory of Extraordinary Optical Transmission through Subwavelength Hole Arrays, *Physical Review Letters*, **86**, 1114-1117, (2001).

[48] L. Martin-Moreno, F. J. Garcia-Vidal, H. J. Lezec, A. Degiron, and T. W. Ebbesen, Theory of Highly Directional Emission from a Single Subwavelength Aperture Surrounded by Surface Corrugations, *Phys. Rev. Lett.*, **90**, 167401 (2003).